Max-Planck-Institut
für Meteorologie

REPORT No. 199

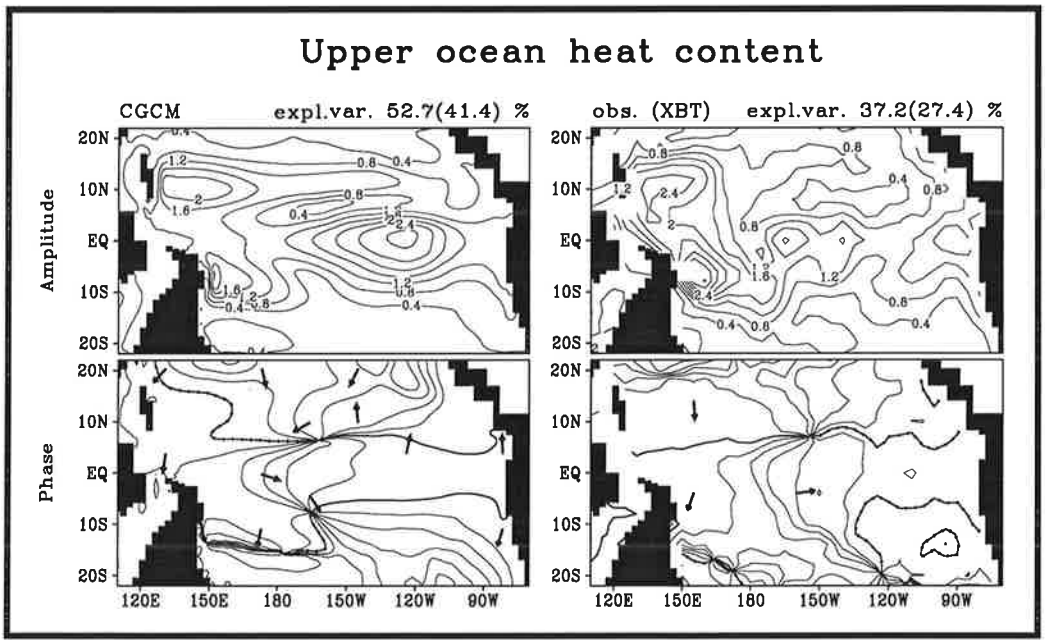

ENSO DYNAMICS AND SEASONAL CYCLE IN THE TROPICAL PACIFIC AS SIMULATED BY THE ECHAM4 / OPYC3 COUPLED GENERAL CIRCULATION MODEL

by

Andreas Bacher • Josef M. Oberhuber • Erich Roeckner

HAMBURG, July 1996

AUTHORS:

Andreas Bacher — Max-Planck-Institute for Meteorology
Hamburg
F. R. Germany

Josef M. Oberhuber — Deutsches Klimarechenzentrum GmbH
Hamburg
F. R. Germany

Erich Roeckner — Max-Planck-Institute for Meteorology
Hamburg
F. R. Germany

MAX-PLANCK-INSTITUT
FÜR METEOROLOGIE
BUNDESSTRASSE 55
D-20146 HAMBURG
F.R. GERMANY

Tel.: +49 - (0)40 - 411 73 - 0
Telefax: +49 - (0)40 - 411 73 - 298
E-Mail: <name>@dkrz.de

ISSN 0937 – 1060

ENSO dynamics and seasonal cycle in the tropical Pacific as simulated by the ECHAM4/OPYC3 coupled general circulation model

A. Bacher[1)], J.M. Oberhuber[2)], E. Roeckner[1)]

[1)] Max-Planck-Institut für Meteorologie,
Bundesstraße 55, D-20146 Hamburg, Germany

[2)] Deutsches Klimarechenzentrum GmbH,
Bundesstraße 55, D-20146 Hamburg, Germany

submitted to Climate Dynamics, May 1996

corresponding author:
A. Bacher, email: bacher@dkrz.de

ISSN 0937-1060

ABSTRACT

The new version of the atmospheric general circulation model, ECHAM4, at the Max Planck Institute for Meteorology, Hamburg, has been coupled to the OPYC3 isopycnic global ocean general circulation and sea ice model (Oberhuber 1993) in a multi-century present-day climate simulation. Non-seasonal constant flux adjustment for heat and freshwater was employed to ensure a long-term annual mean state close to present day climatology. This paper examines the simulated upper ocean seasonal cycle and interannual variability in the tropical Pacific for the first 100 years.

The coupled model's seasonal cycle of tropical Pacific SSTs is in good agreement with the observations with respect to both the warm pool variation and the Central and Eastern Pacific, with significant errors (up to -2 K) only in the cold tongue around April. The cold phase cold tongue extent and strength is as observed, and for this the heat flux adjustment does not play the decisive role; corrections beyond ± 40 Wm^{-2} are rare and only occupy small areas, such as near coasts. A well established south Pacific convergence zone is characteristic for the new AGCM version. Apart from extending the south-east trades seasonal maximum to midbasin, windstress pattern and strength are well captured.

The subsurface structure is overall consistent with the observed, with a realistically sharp thermocline at about 150 m depth in the west and rising to the surface from 160° W to 100° W. The current system is clearly resolved and, on the whole, has expected shape. The equatorial undercurrent is correctly positioned but the core is only half as strong as observed. The north equatorial current and countercurrent also have reduced maximum speeds but the April minimum is captured. The south equatorial current is strong at the equator since the undercurrent has weakened influence.

Like the companion publication (Roeckner et al. 1996) this study finds pronounced tropical eastern and central Pacific interannual variability. Simulated and observed NINO3 SST variability is represented by a single rather broadband maximum of power spectral density, centered on about 28 months for the simulation and four years for the observations. For simulation and observations, SST, windstress, and upper ocean heat content each exhibit a single dominant large-scale amplitude and phase pattern, suggesting the model captures the essential dynamics. The amplitude of the essentially standing oscillation in SST in the NINO3 region attains the observed strength, but is weaker at the eastern boundary. Anomalies of upper ocean heat content show off-equatorial westward and equatorial eastward propagation, the latter in turn arriving in the east of the basin in coincidence with the respective warm or cold SST anomalies. Equatorial windstress anomalies near the date line provide the appropriate forcing and clearly form a response to the anomalous SST.

1. INTRODUCTION

The El Nino/Southern Oscillation (ENSO) is the dominant natural climate variation in the tropics on timescales of a few years. Expressing itself in the recurrent weakening and eastward/equatorward migration of tropical Pacific convergence zones in conjunction with anomalously warm Eastern and Central Pacific sea surface temperatures (SSTs), it also influences extratropical features of the general circulation and ultimately induces a near-global climate signal. In climate models used for the simulation of climate change, the validity of model results pertaining to ENSO is a major concern and should be assessed within present-day climate simulations.

Simulations primarily aimed at studying tropical ocean-atmosphere variability have been done with

coupled ocean-atmosphere models of varying complexity. Models with restricted domain and a simplified atmospheric component but shallow water ocean dynamics or an ocean general circulation model (OGCM) have simulated variability identifiable with ENSO, and were used to formulate the oscillator concept of Suarez and Schopf (1988) and Battisti and Hirst (1989), or the propagating SST modes described by Neelin (1991); see Neelin et al. (1994) for an overview of theoretical concepts and references. *Global* coupled GCMs (CGCMs), of similar type as used in this paper, at the time when Neelin et al. (1992) reviewed coupled modelling of ocean-atmosphere interactions in the tropics had not succeeded in realistically simulating ENSO.

Meanwhile, a number of studies have been published showing results of extended CGCM integrations, with global or near-global extent in both the atmosphere and the ocean component, qualitatively resembling ENSO dynamics more closely although generally with weaker amplitudes than observed (e.g. Lau et al. 1992, Nagai et al. 1992, Latif et al. 1994, Lunkeit et al. 1996, Tett 1995, Knutson and Manabe 1994).

The majority of CGCMs with the entire globe as the active domain in multi-decadal simulations have included flux adjustments (or, 'corrections') (Sausen et al. 1988) in the formulation of the coupling interface. Major motivation includes regional modelling problems, such as an unrealistic seasonal cycle of sea ice or inadequate simulation of the thermohaline circulation in characteristic high-latitude regions, as well as large-scale drift toward a new equilibrium state after coupling the two components, generally following an ocean-only integration toward uncoupled equilibrium. These constant corrections of monthly mean fluxes, generally of heat and freshwater fluxes, and often windstress, sometimes also of SST and ice mass (e.g., Manabe et al. 1991, Cubasch et al. 1992, Lunkeit et al. 1996, Murphy 1995) are designed to constrain the climatology of the model, while ocean and atmosphere interact through anomalies, an approach which generally substantially reduces drift.

When using seasonal flux adjustment, the ability of the model to simulate a realistic seasonal cycle in the tropics is of no fundamental interest. However, the seasonal cycle can have links to ENSO in various ways. Apparently some phase-locking occurs, with the initiation of warm events mostly in Northern hemisphere spring. In an uncoupled OGCM forced by observed winds, Barnett et al. (1992) found that low frequency variability seemed not directly driven by a seasonal cycle but in part of the year the system was more sensitive to perturbations than in the remaining part. In a recent theoretical investigation, Jin et al. (1994), using a stripped-down intermediate model, suggest that the quotient of ENSO and annual periods assumes discrete values given by ratios of small integers, as a model parameter (the coupling strength) is continuously varied, which ultimately leads to chaos. For coupled modeling of tropical atmosphere-ocean dynamics it is certainly desirable to achieve a freely simulated seasonal cycle. A recent comparison of several CGCMs (Mechoso et al. 1995), each integrated over about a decade, was restricted to cases where no flux adjustment was used (longer integrations are described e.g. in Latif and Barnett 1994, 1995 or Robertson et al. 1995a,b). Despite some substantial shortcomings such as a doubling of the ITCZ in some models or its seasonal intrusion well into the Southern Hemisphere in others, as well as a common tendency toward extending the cold tongue significantly into the warm pool, these results certainly represent progress in coupled modelling in the tropics by GCMs, as compared to the earlier review (Neelin et al. 1992).

Here we present results on tropical ocean-atmosphere dynamics obtained with a global atmosphere-sea ice-ocean GCM in the course of a multi-century present-day climate simulation. We have globally applied only annual mean flux adjustment restricted to heat and freshwater, thus leaving the determination of the seasonal cycle up to the model physics. Since in a companion paper (Roeckner et al. 1996) aspects of the simulated atmospheric seasonal evolution and space-time variability connected to ENSO both in the tropics and extratropics are discussed separately, we here focus attention on mod-

el results on the upper tropical Pacific ocean seasonal cycle and interannual variability. The demonstration of the stability of simulated control climate including sea ice, and further aspects of climate variability, will be the subject of forthcoming publications.

The remaining four sections of this paper proceed as follows. First we give a summary of the coupled model and essentials of the coupling strategy. The next two sections are concerned, respectively, with dicussing the simulated upper tropical Pacific seasonal cycle in temperature, currents, and forcing by the AGCM, and with highlighting the spatio-temporal characteristics of the simulated ENSO with ocean response to windstress as the dominant component. Both sections provide comparison with observations. Finally we state conclusions from our present study.

2. GLOBAL COUPLED MODEL AND FLUX ADJUSTMENT

The AGCM and OGCM component, as well as the technique of coupling, represent most recent developments; the coupling of earlier versions of the component models by a different technique, involving seasonal flux adjustment essentially for all quantities exchanged between them, is described by Lunkeit et al. (1996).

The AGCM component is the ECHAM4 general circulation model developed at the Max Planck Institute for Meteorology. It is the current generation in the line of ECHAM models (Roeckner et al.1992) which evolved from the European Centre for Medium Range Weather Forecast (ECMWF) model under extensive reconstruction in parametrizations for processes such as soil processes, local runoff, simple prognostic sea ice skin temperature, boundary layer physics, prognostic cloud liquid water and ice. A summary of recent developments regarding model physics in ECHAM4 and a description of the simulated climate obtained with the uncoupled ECHAM4 model is given in Roeckner et al. (1996). These new features include use of the more recent radiation scheme from the ECMWF model (Morcrette 1991), modified to include additional greenhouse gases, and with revised water vapor continuum absorption (Giorgetta and Wild 1995); introduction of a higher-order turbulence closure (Brinkop and Roeckner 1995); modified mass flux convection and cloud entrainment/detrainment (Nordeng 1995); and a supplement in the stratiform cloud scheme.

The prognostic variables, vorticity, divergence, temperature and surface pressure are represented as expansions in spherical harmonics with triangular truncation at wavenumber 42 (T42). Starting with ECHAM4, advection of prognostic water vapor and cloud liquid water/ice are treated by a semi-Lagrangian scheme. The physical parameterizations run on a 128×64 (lon × lat) Gaussian grid yielding a meshwidth of approximately 2.8°. In the vertical, 19 hybrid σ-p levels are used extending from the topography to 10 hPa. The timestep is 24 minutes except for radiation which uses 2 hours.

The OGCM component is an updated version of the OPYC general circulation model by Oberhuber (1993). It solves the primitive equations in the form of conservation laws for momentum, mass, heat and salt on isopycnal layers, with a realistic equation of state, and the sea level, given by vertical summation of layer thickness at any time, evolving freely. Cross-isopycnal and isopycnal mixing are parameterized, resp., using a Richardson-number dependent criterion and Laplacian diffusion with temporally and spatially varying coefficients. The latter for momentum depend on local Rossby-radius, for scalars on the local deformation of the flow field. The convective adjustment completely removes vertical instability in one timestep.

A mixed layer using the same governing equations as the interior ocean, but with a detailed calcula-

tion of turbulent entrainment/detrainment based on turbulent kinetic energy input by wind stirring, buoyancy flux due to heat and freshwater, and local shear is included as the top layer with an arbitrary potential density and a minimum thickness of 10 m. A fraction of solar radiation is allowed to penetrate below the mixed layer.

Sea-ice and snow-cover is predicted in the form of grid-cell averaged thicknesses and a common area concentration, together with an equation of motion neglecting momentum advection and using viscous-plastic rheology in the stress term (Hibler 1979). A simple computation of ice and snow top temperatures and thermodynamic mass tendencies provides input to the prognostic equations.

In uncoupled simulations, surface fluxes everywhere are given by bulk laws involving observed climatological atmospheric quantities and simulated surface temperature (Oberhuber 1988, 1993), and surface salinity forcing includes Haney (1971) type restoring in addition to precipitation and evaporation.

The diurnal cycle is omitted, and half a day is used in the semi-implicit timestepping. The scalar gridpoints of an Arakawa B-grid coincide with those of the AGCM grid except equatorward of 36° latitude where the meridional spacing is gradually decreased to approximately 0.5° (1.0°) equatorward of 5° (10°) latitude to resolve the equatorial waveguide. Including the mixed layer, 11 layers are used.

The models are coupled quasi-synchronously, exchanging daily averaged quantities once a day. The AGCM receives the mixed layer temperature and the scalar sea ice variables without any correction. For the OGCM, downward solar radiation, river discharge, windstress, and the cube of the friction velocity, u_*^3, are passed, again, without corrections. u_*^3 is passed separately since deriving it from daily mean windstress would lead to underestimation of the turbulent kinetic energy input to the mixed layer. River discharge is computed by the river routing scheme of Sausen et al. (1994) using grid cell runoff as computed in ECHAM. The flux adjustment in heat and freshwater will reflect the difference of flux delivered by the AGCM and flux requested by the OGCM in the long-term annual mean.

For achieving global consistency in the annual mean flux adjustments - including heat flux in the presence of ice -, a suitable scheme was developed (Bacher and Oberhuber 1996). Essentially, in this scheme, the OGCM, as well as the AGCM, both have to supply simultaneous independent estimates of these fluxes during the process of determining the correction (see below) in a coupled integration preceding the main simulation. For freshwater, OPYC uses climatological precipitation and latent heat flux from its bulk parameterization, whereas precipitation minus evaporation is delivered by ECHAM. For heat, the bulk formulae in OPYC are combined with a new formulation for the heat transfer through sea ice and snow cover where these exist, based on analytic temperature profiles and a simple snow melting mechanism. This scheme implemented in ECHAM, too, on sea points ensures a consistent boundary temperature for the lowest atmosphere layer, and, that OPYC is passed net heat flux in ice-free areas, resp. thermodynamic ice and snow mass tendencies elsewhere. The heat flux adjustment then applies to the heat, resp. mass, exchange of the mixed layer with air, resp. ice, above it; snow mass is not subject to heat or freshwater flux adjustments.

In order to spin up the OGCM, approximately 1000 years of ocean-only integration were conducted. Over the first 500 years observed climatological quantities, such as air temperature, entered the bulk laws in OPYC, except taking the windstress from an uncoupled integration of the ECHAM3 AGCM with observed SST from 1979 - 1988 (ECHAM4 was still under construction). Subsequently, day-to-day variability of net heat flux and precipitation minus evaporation anomalies from ECHAM3 was added.

Next follows a transition phase of coupling with continuously updated flux adjustments. Denoting F_A the flux - heat or freshwater - passed by the AGCM, F_O the flux resulting from the OGCM bulk parameterization under the same surface conditions and F_{rest} an additional Haney (1971) type restoring term (zero for heat where ice exists), the flux F seen by the OGCM in the final phase (fixed flux adjustment) is

$$F = F_A + << F_O + F_{rest} - F_A >>$$

where the second term on the right represents a long-term annual mean. The transition phase is used to initially estimate this term on a daily update basis and then smoothly relax to only annually updated estimates in the form of averages over all completed years. For both flux adjustment fields, extending the transition phase over 100 years yielded sufficiently well defined expectation values of the sequences of yearly updates, despite tendencies for local cyclostationarity in the freshwater flux adjustment estimates. The fully coupled run with corrections fixed was then initialized with the state at the beginning of year 91.

Since in the tropics the two model grids differ as stated above, particular care has been taken to convert the fluxes passed by the AGCM in a conserving way. A numerically efficient scheme has been developed which respects positivity, e.g. for u_*^3 or river discharge, and guarantees exact local conservation. A more detailed description is given in Bacher and Oberhuber (1996).

3. SEASONAL CYCLE

The upper ocean seasonal cycle simulated by the CGCM is of interest since only the annual means of the fluxes of heat and freshwater undergo flux adjustment. The wind-driven upper ocean circulation is not affected by flux adjustment, and the SST also feeds back fully to the atmospheric circulation (omission of windstress adjustment leaves only secondary possible feedbacks on wind-driven currents by the effect of heat flux adjustment on SST). In this section, we give an account of the mean annual cycle of the surface temperature, net heat flux and windstress, and upper ocean temperature and currents, primarily as a background for the description of interannual variability in the subsequent section.

3.1. SST

Fig. 1 shows the observed and simulated sea surface temperature (SST) for all three oceans. For the simulation, the first 100 years (91-190) were used. The observations are taken from the global ice and sea surface temperature (GISST) dataset, version 2.2 (Rayner et al. 1995), for which each month was averaged over the period 1951 through 1975.

In the tropical Pacific, the observed annual cycle is strongest in the east, where the equatorial cold tongue has minimum strength in the month of April and is strongest in September. For the western Pacific warm pool, annual/semiannual cycles imply that the proportion north of the equator of the region of maximum SSTs (> 28°C) is only minor for January through March but major for July through September. Our choice of four months includes April and October as found in a recent study comparing coupled GCM results in the tropical Pacific (Mechoso et al. 1995). The inclusion of January and July (cf. e.g. Horel 1982) permits limited reference to the phasing of the seasonal cycle when comparing simulation and observations. For the cold tongue, in July and October there is good agreement. The

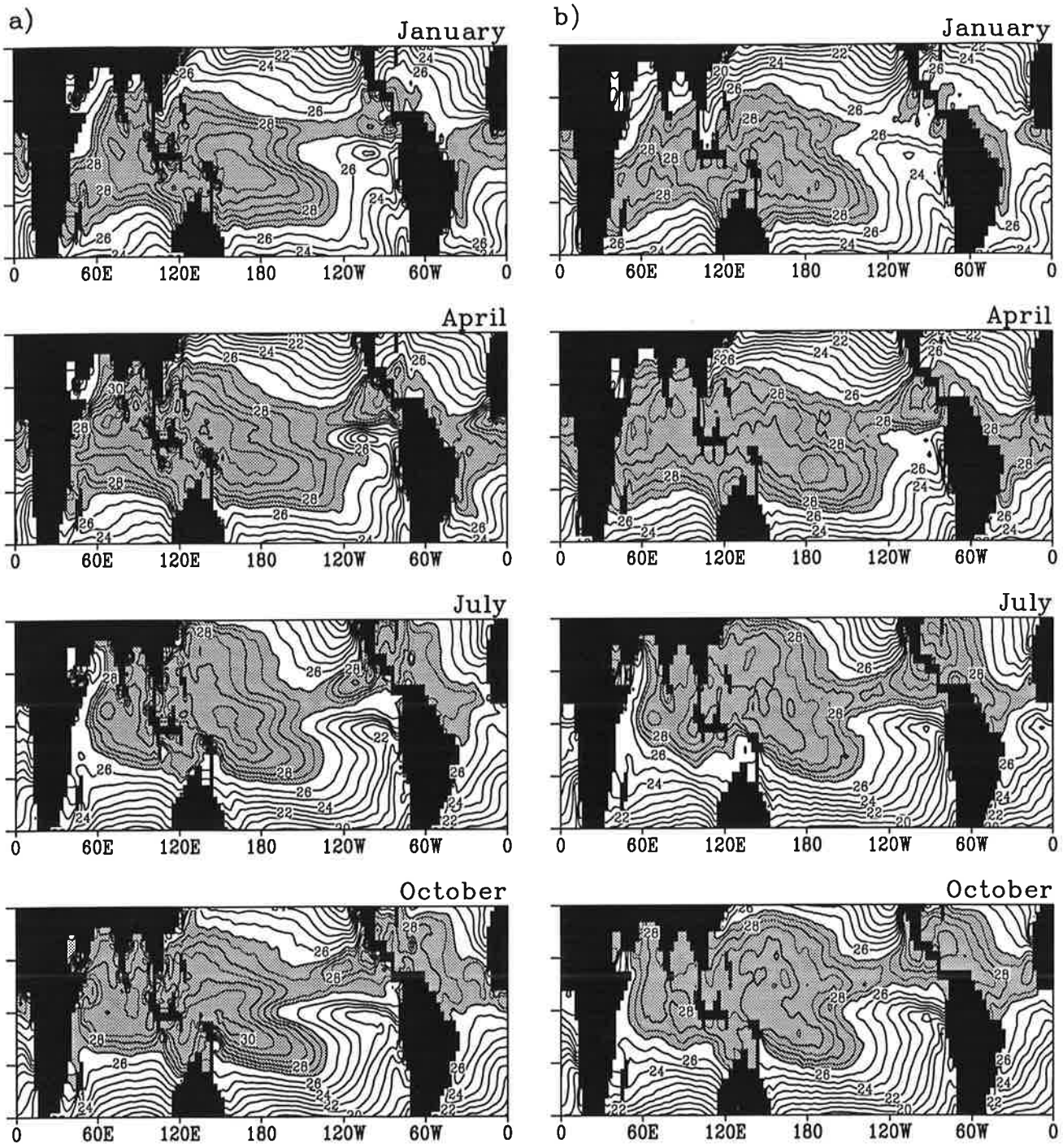

Fig. 1. Monthly mean SST (January, April, July, October), a) coupled model, yr 91 - 190; b) GISST 2.2 data, 1951 - 1975. Contour interval 1 K, additional thin contours at 0.5 K intervals above 27° C, this temperature range is additionally shaded. The model land-sea mask is shown in all figures displaying maps however not implying regridding of observed data. For the GISST data, used here after transformation to T42 resolution, all analyses have also been done using the original dataset at, nominally, 1°× 1°, yielding a perfect match for fig. 1 and fig. 10 (resolution will perhaps matter more at any particular date)

south-eastern extension of the region warmer than 27°C is limited at about 120° W, and the simulated westward extent of the cold tongue matches the observed. For January, the 26°C and 25°C isotherms as simulated, roughly coincide with the 25°C and 24°C isotherms in the observations, resp., except for a small equatorial region near 110° W, where 24°C are simulated and observed. This is also where the largest errors are found in the comparison of all SST plots, namely in April when the seasonal maximum is missed by more than 2 K in this spot. Not many of the current coupled GCMs correctly reproduce the boreal spring temperatures in the cold tongue (Mechoso et al. 1995, Robertson et al. 1995), though some also underestimate them in boreal fall, thus yielding a colder mean state but alleviating errors in the seasonal deviation. For the warm pool, rather close agreement is found for all months shown, although there is an indication that in July and subsequently the NH portion of waters above 28°C attains less north-eastward extent, as well as a premature southward migration suggested by comparing July and October.

3.2 Heat flux

Some of the features in the simulated SST can be related to the atmospheric forcing by windstress and net heat flux, i.e. the sum of long- and shortwave net radiation and latent and sensible turbulent fluxes. The present discussion also covers the flux adjustment for heat (Fig. 2.e)). In the determination of the seasonal cycle of the upper tropical Pacific the forcing by windstress and heat flux dominates over precipitation; the latter has been shown as annual mean by Roeckner et al. (1996). Fig. 2.a) through d) show a comparison with Oberhuber's (1988) estimates of net heat flux for the extreme months of January and July and the annual mean. The general agreement is quite satisfactory, bearing in mind the sparsity of measurements in the south-eastern subtropical Pacific, particularly in July. Wavelike structure in the simulation results originates from the truncated spectral representation of the orography including the sea surface in the AGCM. In the area between Papua New Guinea and the date line, a difference of around 30-40 Wm^{-2} is seen. In the west Pacific warm pool region, we can thus to some extent relate the required flux adjustment heat input to the forcing by the AGCM. From first inspection of individual components and analysis of an uncoupled integration of the AGCM (Chen and Roeckner, 1996a, b), stronger than observed latent heat flux or high cloud albedo is likely to be the primary contribution. However, these publications have used different observed heat flux datasets which indicate heat flux closer to zero in the equatorial western Pacific than estimated by Oberhuber (1988). The rather homogeneous distribution of heat flux adjustment in the North Pacific with heat input of 30-40 Wm^{-2} required does not have a counterpart in the present comparison of simulation and observational estimates. Since the bulk parameterizations in the OGCM are very similar to those used in the present observed estimates, we attribute this to the contribution of averaged F_{rest} to the flux adjustment. In the core of the cold tongue, the AGCM heat flux exceeds observational estimates by about 40 Wm^{-2}, consistent with a shifted heat balance by reduced latent heat flux due to the cold bias in SST primarily in northern spring. Overall, despite leaving room for improvement, the quantitative comparison of net AGCM heat flux with the observed estimates appears reassuring. So is the fact that the non-seasonal heat flux adjustment, having typical magnitudes at the lower end compared to other (seasonally) flux-corrected CGCMs (e.g. Tett 1995) does not show strong spatial structure, e.g. over the annual mean cold tongue (north of which there is only a shallow minimum).

3.3 Windstress

Fig. 3 shows January and July mean windstress for the simulation and pseudo-stress for 1970 through 1994 and 1961 through 1994 in the Indian and Pacific oceans, resp., from the FSU atlas (Stricherz et al. 1992, 1993). These months are used for consistency with the above discussion of SST and net heat flux, although the observed windstress in the south-eastern Pacific increases by about a further 10 per-

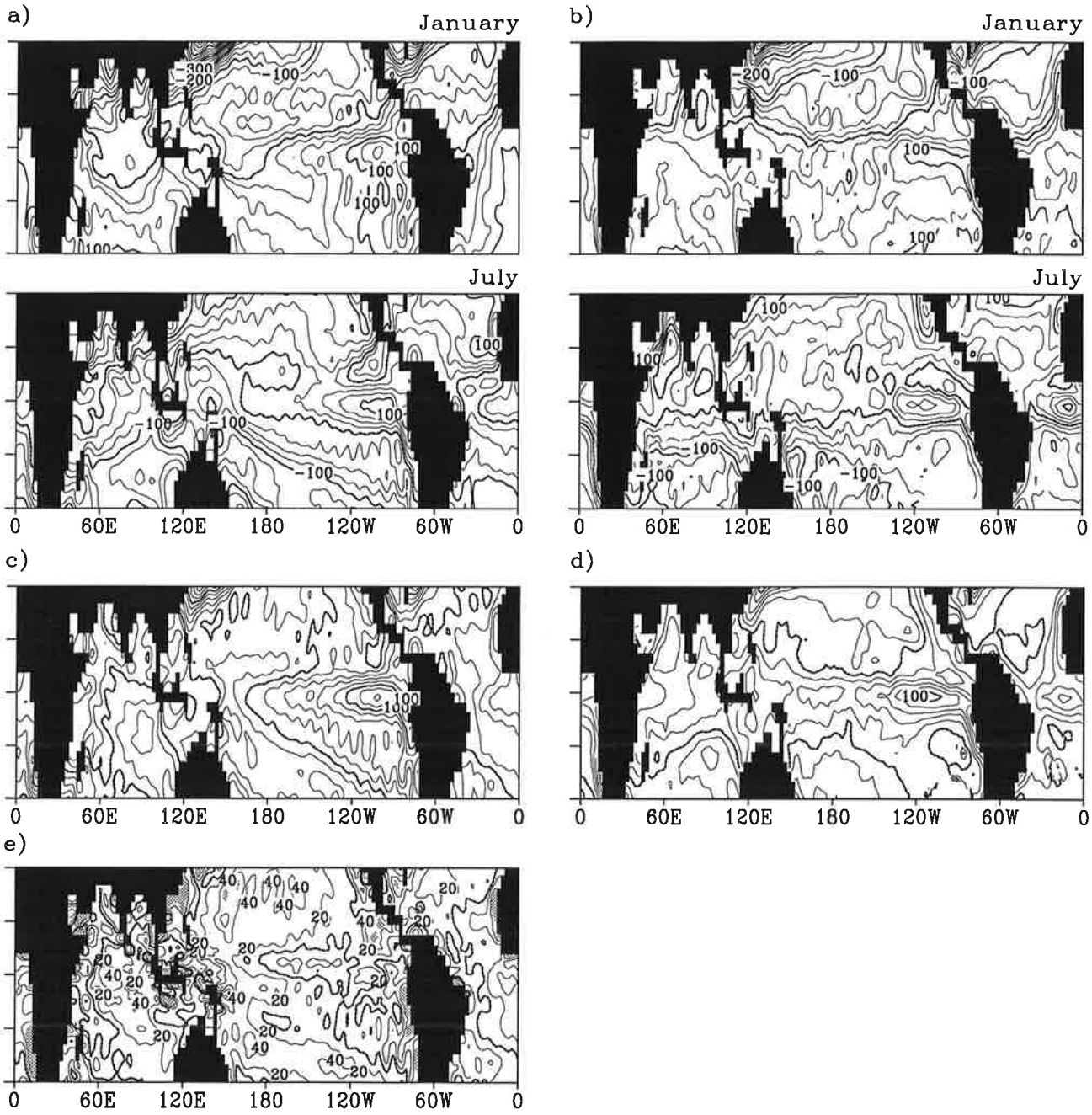

Fig. 2. Mean net heat flux a) as passed from AGCM un-flux-adjusted, for January and July; b) Oberhuber climatology for January and July; c) as a), annual mean; d) as b), annual mean; e) heat flux adjustment. Contour interval 25 Wm^{-2} for a), b), 20 Wm^{-2} for c), d), and e). In e), shading indicates values beyond ±60 Wm^{-2}

cent from July to August, with a concomitant decrease in the NH at about 15° N. In the simulation there is less difference between July and August. Since the FSU stress is given without air density and drag coefficient, we performed a comparison for the CGCM data by computing approximate average values of squared 10 m windspeed over simulation years 121 through 150, using the twice-daily output of instantaneous wind velocity for the lowest layer and the roughness length. On dividing the proper windstress, accumulated from all timesteps, by this square windspeed estimate, the resulting product of air density, and drag coefficient over most open ocean areas shown here deviates from

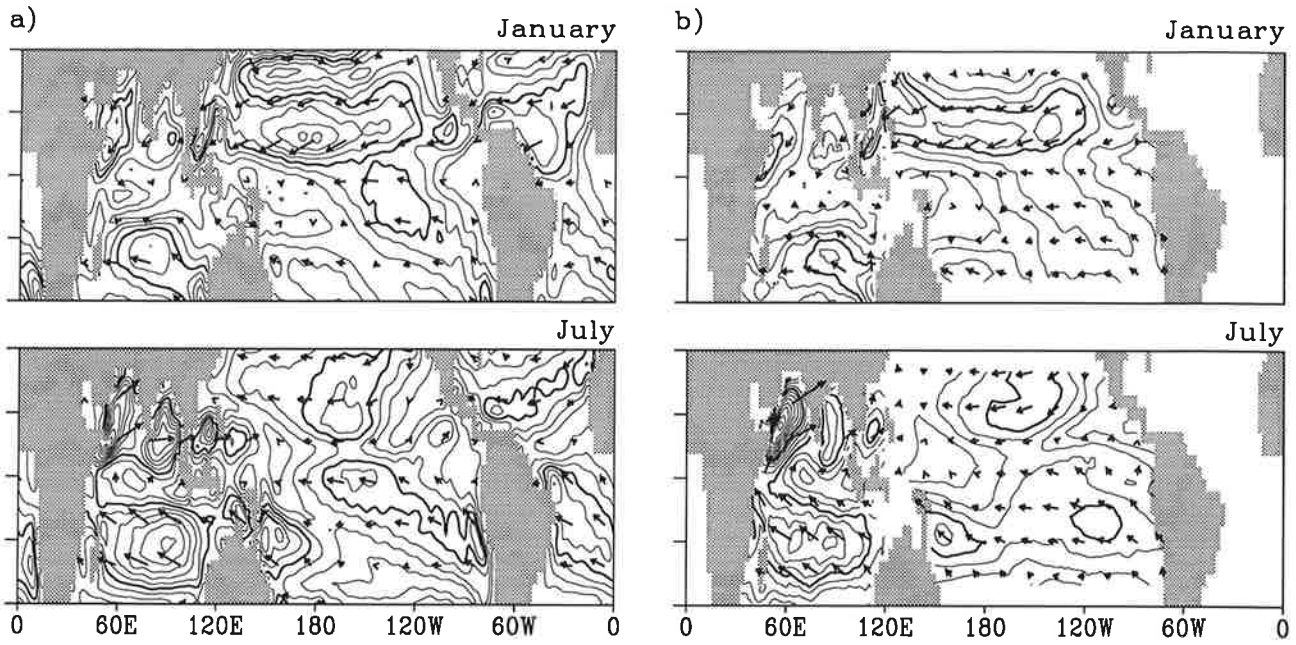

Fig. 3. Mean wind stress a) coupled model, for January and July; b) FSU data for January and July, multiplied by 1.5×10^{-3} kg m^{-3}. Contours for magnitude at intervals of 0.02 Nm^{-2}; thick contours for 0.08 Nm^{-2} (and multiples thereof)

about 1.5×10^{-3} kg m^{-3} by at most 15 percent. To ease comparison, this was applied as a constant factor to the FSU pseudostress. For January, simulation and observations show good agreement, with a tendency for slightly stronger winds in the model.

For July, stronger observed winds are found over the Arabian Sea, while in the Pacific the SH maximum in the simulation is extended north-westward in relation to the observed distribution. Nevertheless, the agreement is still good; in particular, the wind strength is reduced realistically towards the western equatorial Pacific, along with a realistic slanting of the SPCZ. A problem in several coupled GCMs has been that the region of convergence tended to evolve into a narrow zonal cross-basin shape south of the equator mirroring the ITCZ, particularly in integrations without flux adjustment (Mechoso et al. 1995). In the present AGCM version a modified closure in the cumulus convection scheme linking penetrative convection to convective available potential energy (CAPE) rather than moisture convergence is used (Nordeng 1995). This results in a closer link of convection to forcing by SST and reduced winds over the equatorial Pacific portion of the warm pool, a benign effect if the cold tongue tends too far west (see also the conclusions in Roeckner et al. 1996). Test integrations with our OGCM coupled to ECHAM3, both the standard version and after implementing the ECHAM4 cumulus convection as the sole modification, confirmed the improved patterns of winds and convection.

3.4 Vertical structure

For the following account of vertical temperature and current distributions it is important to treat the layer-based variables in accordance with the conservation laws expressed in the OGCM equations. At each timestep we employ a transformation algorithm from isopycnal to space-time-invariant Z-layers which at each (x,y) location preserves vertically integrated $\rho \times \Psi$ where Ψ is T, u, v. Thus, to the staircase-function profile of $\rho \times \Psi$ we apply an integral-preserving quadratic spline fit below the mixed

layer and subsequent analytic vertical integration over the new Z-layers, whose midpoints correspond to the depths of the Levitus (1982) dataset. The spline assumes isopycnal number rather than mid-point depth as the independent variable, implying vertical stretching of sharp gradients which greatly reduces the tendency for wavelike overshooting of the fit (although spurious waves for T are still discernible above and below the 21°C isotherm e.g. in fig 4.a) and e)). Subsequently inverse vertical stretching restores integral conservation, sacrificing continuity of the vertical derivative. But the algorithm avoids large zero-order discontinuities as would result if Z-layers were simply assigned values from corresponding isopycnal layers with linear weighting near isopycnal interfaces, given the mapping of eleven layers into 33 Z-layers. The upper 350 m in the tropics are typically covered by the mixed layer and five isopycnal layers which transform into 12 Z-layers.

After time-averaging the transformed $\rho \times \Psi$ and ρ, the quotient yields mass-weighted temperature and currents and vertically integrated mass flux divergence divided by density, representing vertical velocity but including exchange terms such as by convective adjustment. Sections along the equator and along 150° W of the so defined temperature, horizontal currents and vertical velocity are shown in fig. 4 and 5.

As follows from the discussion of the seasonal cycle of model SST, in the zonal sections of temperature for April and October (fig. 4 a),e)), near 110° W too many isotherms reach the surface in boreal spring. The magnitude of the vertical velocity (fig. 5.c)) and the absence of a strong maximum cannot fully explain this very localized SST feature. An inspection of the layer thicknesses and mixed layer heat budget terms (not shown) leads us to at least partly ascribe this to the vertical temperature gradient, i.e. to very cold water being entrained into the mixed layer from the next non-vanishing subsurface layer. However, the simulation otherwise successfully reproduces observational features such as a sharp thermocline at about 150 m depth in the west with upward sloping isotherms east of about 160° W and a greater equatorial eastward extent of the warm pool in April. Comparing to the Hawai to Tahiti shuttle data (Wyrtki and Kilonski 1984) the meridional section (fig. 4.b),f)) shows that even the relativley few upper ocean layers through the freedom to adjust their local thickness manage to capture the observed structure quite well above 300 m. As expected from SST, the asymmetry about the equator is more marked in April than in October.

Using geostrophic arguments modified near the equator as suggested by Picaut and Tournier (1991), the meridional section of the zonal current (fig. 4.d),h)) appears consistent. In particular, as described variously (e.g. Reverdin et al. 1994 and references therein), the North Equatorial Current (NEC) and the North Equatorial Countercurrent (NECC) are both weak in April. The Equatorial Undercurrent (EUC) appears to have the core in correct position but underestimated by almost a factor of 2; the same reduction as apparent with the seasonal values of the NECC and NEC. The latter may also show effects of the variable meridional grid spacing which increases from about 0.7° at 5° N to 1.5° near 15° N. Latitudinally the simulated EUC is wider than observed. At present we have only a tentative explanation, namely the momentum diffusion coefficient, although somewhat dependent on horizontal resolution, cannot assume sufficiently low values, hence the spreading out of the effect of the correctly simulated zonal density gradient. In terms of reducing the nonlinear effect of zonal momentum on the surface this could also explain the strength of the South Equatorial Current (SEC) near the equator, with only slight reduction in April when there is also no outcropping of the EUC further east (fig. 4.c),g)).

The meridional velocity at 150° W (fig. 5.b)) is given as annual means corresponding to the display of observations for this quantity in Reverdin et al. (1994). The strength is acceptable, but the asymmetry in the mean state is not well supported by the observations. This to first order appears consistent with the extension of the seasonal maximum of the south-east trades to midbasin which there induces the

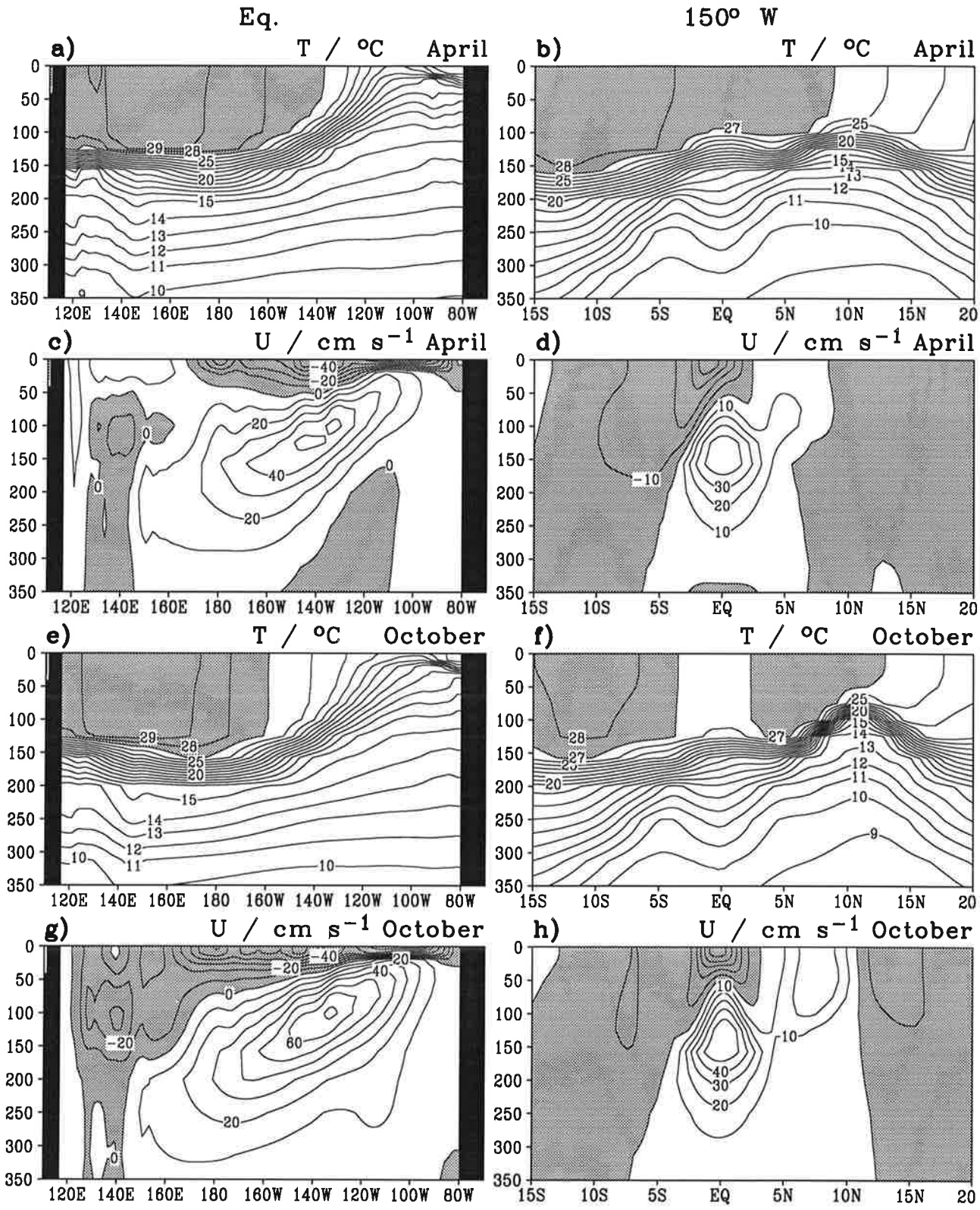

Fig. 4. a) temperature section along the equator for April; b) meridional temperature section at 150° W; c) section of zonal velocity along the equator for April; d) meridional section of zonal velocity at 150° W; e), f), g), h) as a), b), c), d), but for October. Contours at intervals of 1 K for temperature and at 10 cm s^{-1} for velocity; stippling indicates regions warmer than 27° C, resp., where motion is westward

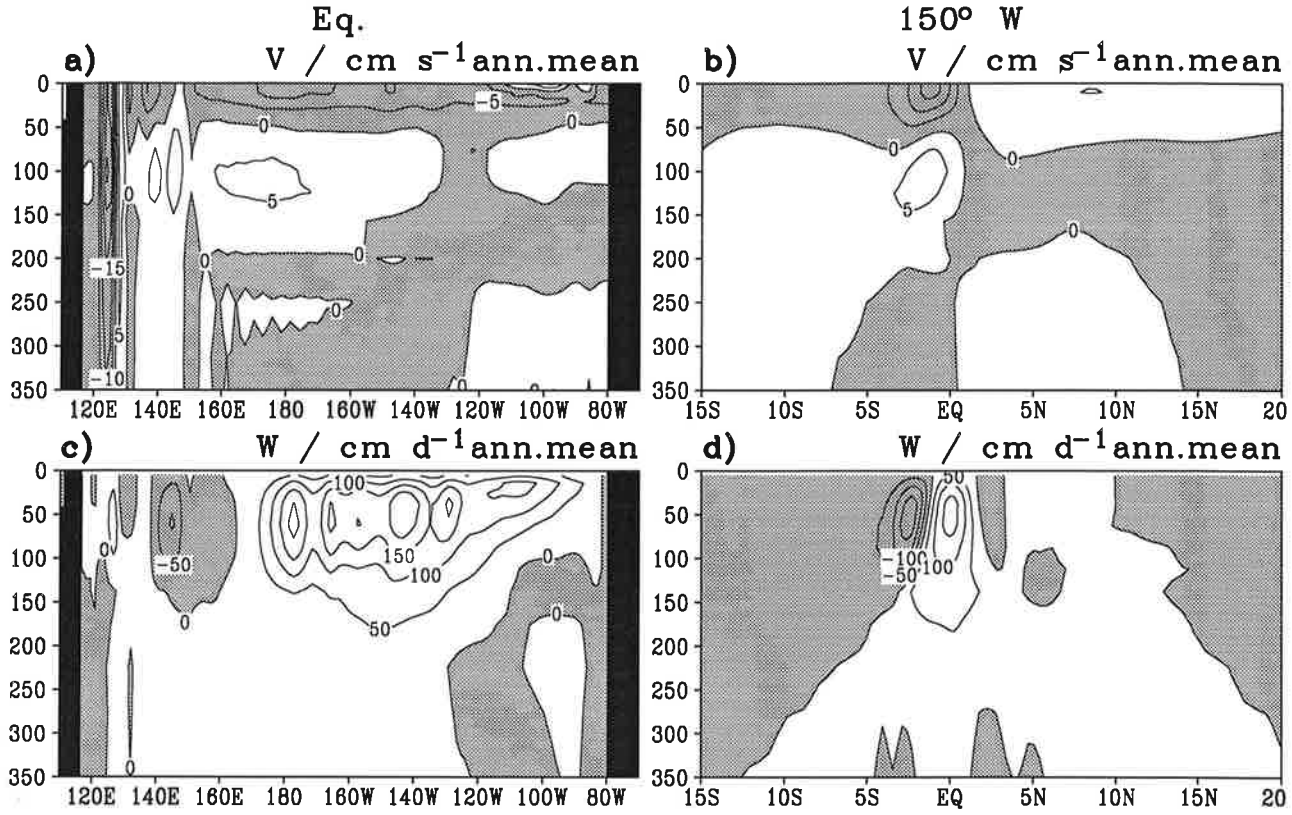

Fig. 5. a) section of annual mean meridional velocity along the equator; b) meridional section of annual mean meridional velocity at 150° W; c), d) as a), b), but for vertical velocity. Contours at intervals of 5 cm s^{-1} for meridional velocity and at 50 cm d^{-1} for vertical velocity; shading indicates regions of southward, resp., downward motion

absence of the observed north-eastward slanting of the zone of minimum windspeed associated with the ITCZ in this season (this can also be anticipated by comparing July in fig. 3). Thus, the NECC and NEC tend to have near zero meridional component. Still, the equator is the region for the well defined meridional maximum of vertical motion which is dominated by the meridional divergence term and is confined in a region close to the surface (fig.5.d)). Off-equatorial downwelling regions correspond to the upwelling on the equator. Overall, as with temperature, the tropical upper Pacific current structure represents a subtle aspect which our global CGCM captures well.

4. ENSO-RELATED DYNAMICS

4.1 NINO3 variability

The first inspection of ENSO-like behaviour involves the timeseries of anomalous SST, averaged over the NINO3 region. The simulated timeseries and that obtained from the GISST 2.2 dataset are shown as unfiltered monthly means in fig. 6.a) and b), respectively. We note several similar aspects of the two timeseries. First, the model seems to produce a signal of similar strength as seen in the observations. Both series show variance fluctuations up to long timescales. Thus, from the seventh decade of the simulation (year 151 onwards) the amplitude seems overall stronger than in the earlier part, while the signal strength in the observed record seems less before ca. 1950 with an apparent

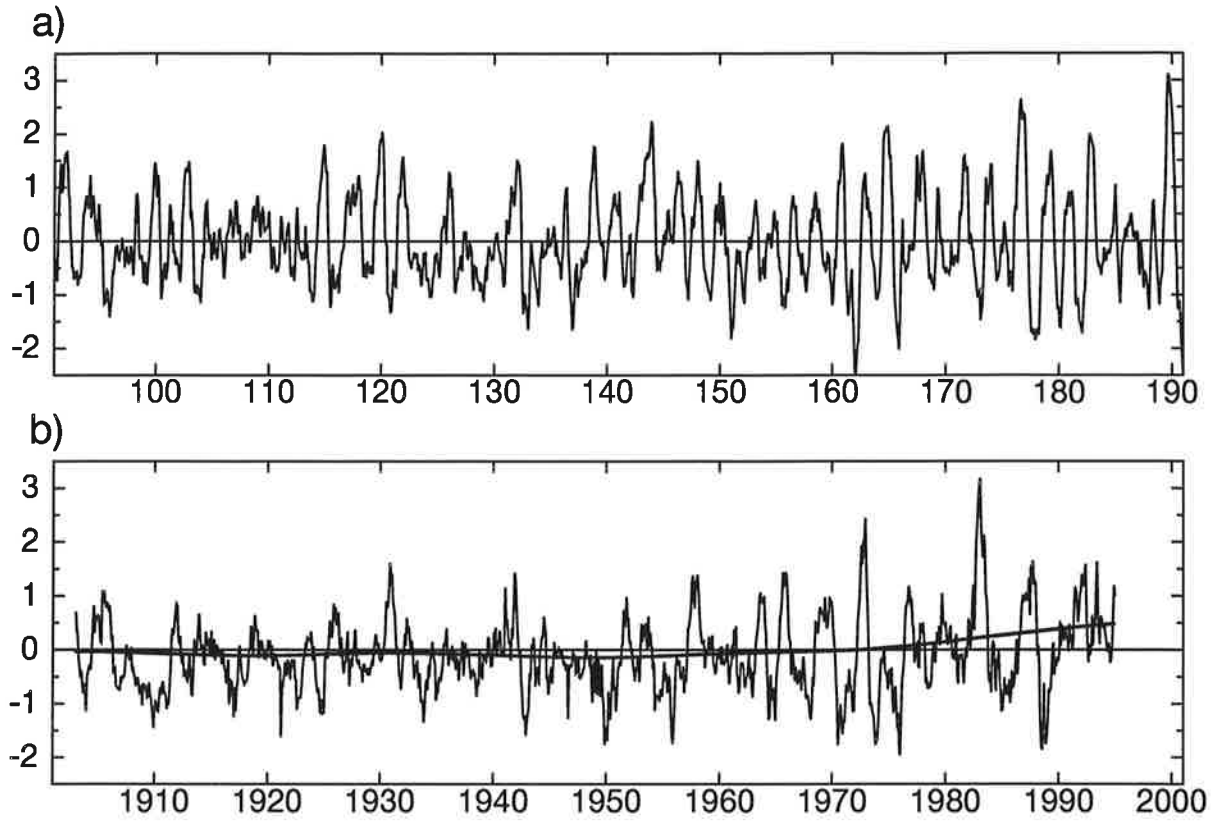

Fig. 6. average SST anomaly NINO3 region, a) coupled model, b) GISST 2.2 dataset. In b), the thick curve shows trend and marginally resolved multi-decadal variablility as output by filtering with frequency response shown as the left curve in fig. 8. Ticks mark the beginning of a year

strengthening in the last three decades. The two strongest warm excursions in the GISST data, the 1972/73 and the 1982/83 ENSO events influence the appearance considerably; disregarding them the evolution of variance would appear more uniform. (Of course, if anything, a smaller amplitude, or more noise, in the earlier period than in the latter should be expected from deficient resolution and temporal non-uniformity of the measurements.) Also, both series show extended periods where the signal seems absent, e.g. over a decade in the simulation starting from year 103, or from 1933 through 1940 and 1943 through 1949 in the observations. In the model results the warm-cold succession from about year 142 onwards appears more regular than before.

Both simulated and observed variability appears dominated by interannual timescales. In the remainder of this section we present, for both, temporal and spatial characteristics with emphasis on the spatio-temporal pattern evolution. Since it emerges that this can be statistically captured by a single, strongly dominant pattern whose time evolution is more appropriately viewed as distributed over a single broadband spectral maximum, the term 'timescale' is somewhat vague. As the time evolution of the emerging SST patterns closely resemble fig. 6, we continue by a characterization of timescale in terms of power spectral densities (PSDs), fig. 7, of the NINO3 timeseries.

Concerning trend removal, in the simulation the trend is insignificant; a straight line fit is subtracted. For the observations, linear de-trending insufficiently removes very low frequency power, with adverse effects, such as power leakage, on the spectrum estimate. Instead we subtract the output of a low-pass filtering by an algorithm identical to that in section 4.3, where half-power at one year will be

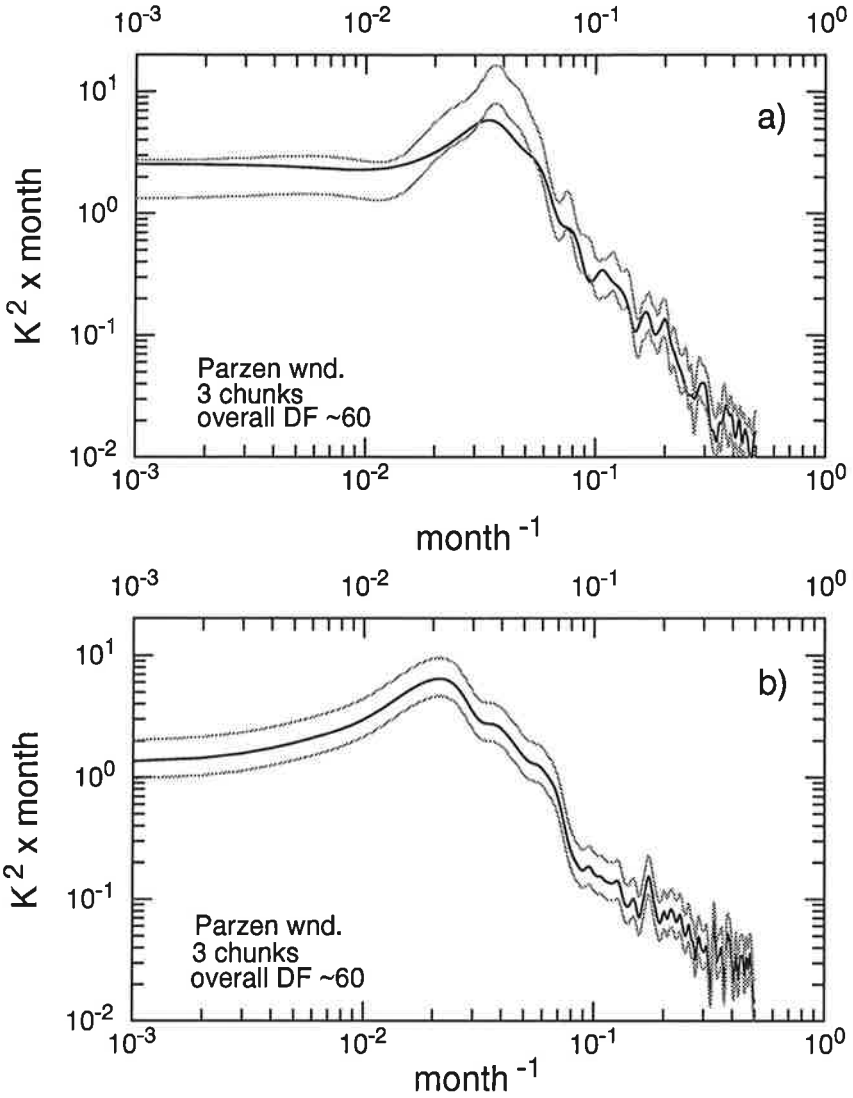

Fig. 7. Power spectral density of unsmoothed average SST anomaly NINO3 region, a) coupled model, b) GISST 2.2 dataset, after eliminating unresolved low frequency variability and trend

used. For de-trending we use half-power at 1/(50 year) as follows: i) smoothing cubic spline (Reinsch 1967), zero third time derivative at start and end; ii) MA-filtering with weights from truncated impulse response of the smoothing spline; iii) use of full infinite impulse response, modified to give a (theoretically) stable ARMA filter, to predict values towards start and end not obtainable in ii); iv) average i) and the result of ii),iii). The spline was not directly used to evade the strong distortion of the fit towards the ends of the input data, resulting from the very low half-power frequency. The filter transfer function, fig. 8, is purely real (filtering preserves phase) and unity over a continuous frequency range including zero frequency (mean and trend); in the case of FFT only two discrete sinusoids would have appropriate frequency for the desired low pass.

After de-trending a Parzen (1961) window was applied to the sample autocovariance which in turn was separately computed over several non-overlapping segments (chunks), subsequently the respective periodograms were averaged. 2.5 % / 97.5 % confidence limits always apply to the full length of the respective series. By contrast, for the simulation the full line shows the PSD for the first six decades only. This yields a restatement that for later years the simulated signal strength increases.

At the high-frequency end both spectra are compatible with an inverse-square law as expected for red noise. At the present resolution both PSDs have a single broad peak which is at about 4 years for the

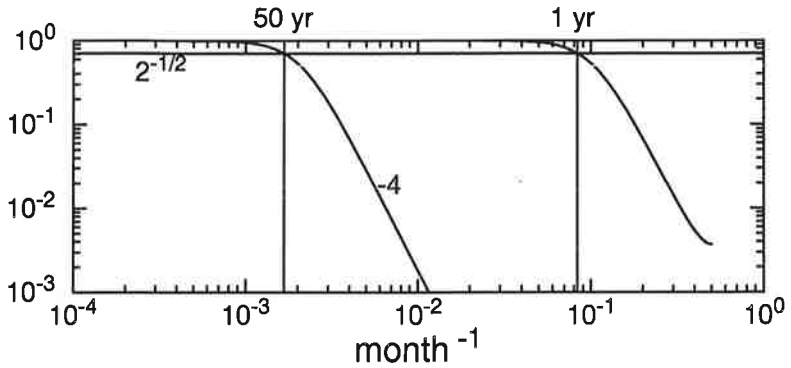

Fig. 8. Filter frequency response used for obtaining the thick curve in fig. 6.b) (left response curve), resp., for light smoothing of data prior to the analyses illustrated in fig. 10 to 12 (right response curve)

observations and at about 28 months in the simulation. We stress that substructure of each peak is a possibility, but only a much greater record length would permit the unambiguous discrimination of such a multimodal signal against a broadband process suggested by fig. 7.a),b). We performed a simple test with an AR(2) process of similar bandwidth driven by white Gaussian noise and found that, unless the χ^2 degrees of freedom of spectral smoothing was set as high as 230, in the estimated periodogram the true peak was split in two, apart from other spurious peaks, however apparently supported by the confidence limits. If the true spectrum actually is broadband, any spectrum estimator (e.g. Maximum Entropy method) is likely to misrepresent it (Kay and Marple 1981), in other words, a group of peaks may represent more broadband structure. On the other hand, failure to resolve two neighboring sharp peaks is also possible, thus neither the single peak null hypothesis nor alternatives can be rejected with confidence. Methodically we thus note difficulties with the unambiguous identification of the often-cited bimodality in ENSO variance (Rasmusson et. al. 1990, Latif et. al. 1992). In fact Barnett et al. (1995) have noted that the so-called low-frequency mode has had a timescale attributed by various authors whose estimates spanned roughly a factor of two, and computed estimates from 26 to 40 months, which was part of their motivation subsequently to prefer the term 'Principal Spatial Mode'. Subsequently we demonstrate that although the observed variability, whether broadband or bimodal, doubtlessly peaks at longer period than simulated, the latter has space-time characteristics remarkably similar to observations.

4.2 Equatorial/off-equatorial zonal evolution

Before entering the direct comparison, we examine the simulated tropical space-time variability in all three oceans in fig. 9.a),b) showing Hovmoeller plots of unsmoothed monthly mean anomalies of SST and heat content of the upper 350 m averaged over the indicated latitude bands. The heat content was computed as the vertical integral of $\rho \times T$, which after the layer remapping reduces to a simple vertical summation. The first and the last sixteen years of our analysis period are shown. Although portraying essentially the same dynamics, the latter period has a clearer and stronger signature. In the Pacific, equatorial SST anomalies develop in place, with no significant zonal propagation evidenced. Near the Peruvian coast, as a rule the amplitude is reduced, resp., relatively insignificant apart from the time close to the largest excursions found in the longitude range corresponding to the NINO3 region. In that range over the latter period, despite the peaks in year 179 and 181, resp., occurring around northern spring, a general preference is seen for the maximum to lie in the second half of the year. The

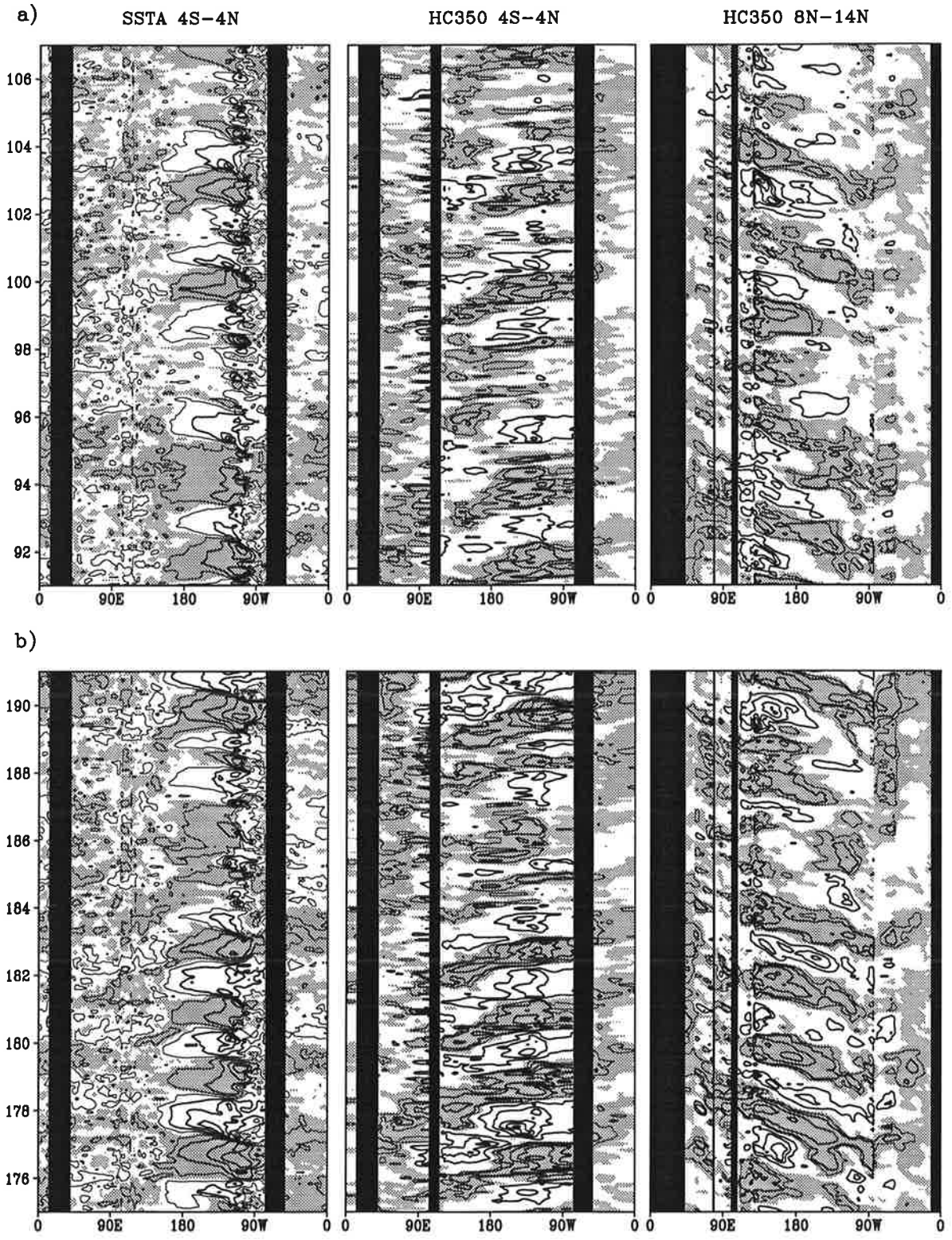

Fig. 9. a) Hovmoeller diagram of unsmoothed monthly mean anomalous SST (left) and heat content of the upper 350 m (centre and right), averaged over latitude bands as indicated, for simulation yr 91 - 106; b) as a), but for simulation yr 175 - 190; contours at intervals of 1 K, 20 kg K cm^{-2}, resp. Thin contours indicate ±0.3 K, 10 kg K cm^{-2}, resp. Shading indicates positive anomaly. Ticks mark the beginning of a year

spring peaks tend to be an extension where already strong anomalies of the preceding year appear further enhanced. Sometimes, e.g. 182/183, the peak encompasses the turn of the year. These findings indicate moderate phase-locking to the seasonal cycle.

In about one third of the warm peaks in the latter period, the anomaly exceeding 1 K is confined to a relatively small longitudinal extent, e.g. year 175 or 184. Corresponding to all more extended warm events and most others we observe an eastward-propagating signal in equatorial heat content. Thus about six months in advance of the SSTA peak, positive heat content anomalies are seen at the western boundary of the Pacific. For the more longitudinally confined SSTA cases, the apparent propagation speed is larger (e.g. year 184), and in the eastern half of the basin at any longitude a shorter duration of anomaly is observed. On the other hand, more spatio-temporal fine structuring of the equatorial signal is apparent in advance of the more extended SSTA excursions. In these cases the westward propagating off-equatorial heat content signals most clearly appear as precursors to the equatorial eastward propagation. The time for crossing the basin near 10° N is typically about one year.

Altogether this picture is consistent with results from many coupled models with high OGCM resolution, as far back as that of Schopf and Suarez (1988), and with spatio-temporal characteristics of observed ENSO as described in Latif et al. (1992). El Nino type eastern and central Pacific SST variations dominate our model's tropical interannual variability and are linked to equatorial wave dynamics with emphasis on the first few baroclinic modes, but with several equatorial waves superimposed in most ENSOs, hence the fine-structuring of signals. Although this complexity precludes a detailed examination of the dispersion relation, the free modes available for producing the simulated dynamics in a linearized treatment are eastward equatorial Kelvin and westward off-equatorial Rossby waves, which latter reflect at the western boundary into equatorial Kelvin signals with downwelling or upwelling character matching the incident wave. To form a self-sustained oscillation, a closed feedback loop involves eastern equatorial SST modified by arriving Kelvin waves, windstress responding to SST changes and forcing oppositely signed off-equatorial Rossby waves, a scenario presented in its simplest, point-coupling and single-mode, approximation by Suarez and Schopf (1988) and similarly by Battisti and Hirst (1989). Patterns emerging from our analysis below, including zonal windstress, are consistent with this general type of feedback.

The Atlantic shows much weaker variability than the Pacific, but in equatorial heat content some lagged coherence with the Pacific is seen for the mentioned larger scale/stronger type of SST anomaly. For the Indian ocean a dynamic link with the Pacific is not obvious in this spatially restricted representation.

4.3 Interrelation of dynamic forcing and thermal structure

We will now obtain a less spatially selective description than is possible by Hovmoeller diagrams along latitudes (indeed reaffirming the choice of latitude), and include observed data. We concentrate on anomalous SST, zonal windstress, and upper ocean heat content as the most important combination characterizing atmospheric forcing and ocean response on interannual scales (e.g. Neelin 1991, Latif et al.1992, Schneider and Barnett 1995). Our aim is to decompose variability into spatial amplitude and phase patterns with respective coefficient time series. For each variable we separately estimate complex empirical orthogonal functions (CEOFs; Barnett 1983, Horel 1984). This concept was originally derived from frequency domain principal component analysis (FDPCA, e.g. Brillinger 1981) where for a multivariate timeseries the spectrum matrix is diagonalized at various frequencies. Equivalently in the time domain, the timeseries, narrowly bandpass filtered, can be made complex-valued by adding as the imaginary part the result of advancing it by a temporal phase of 90 degrees. The complex-valued multivariate timeseries is then EOF-analyzed. With CEOFs one widens the bandpass or

effectively omits it and uses 90 degrees lead in all Fourier components. In this broadband setup the method imposes no periodicity constraint as with each FDPC, however, if some frequency range is associated with maximum variance/spatial autocovariance, the leading pattern can capture the signal.

Fig. 10.a),b) shows the leading CEOFs and associated principal components for the model and the GISST data. The filtering consists solely of the trend removal mentioned above and a lowpass of the

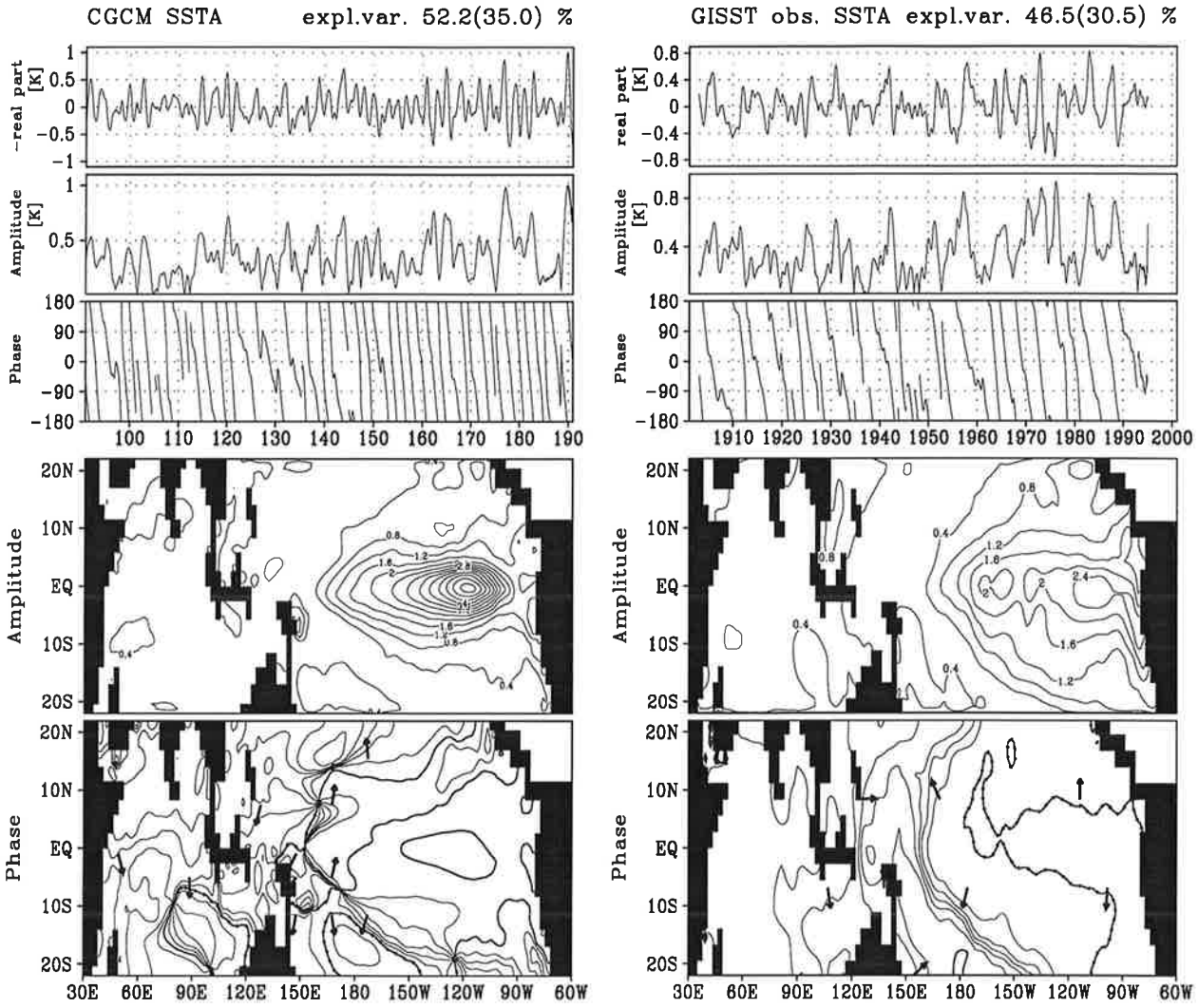

Fig. 10.Anomalous SST leading complex empirical orthogonal function (CEOF) (bottom 2 panels) and principal component time series real part, amplitude and phase (top 3 panels), a) coupled model, b) GISST 2.2 dataset. CEOF amplitude is dimensionless; CEOF phase contour interval is 30°, with 0° and 180° bold, additionally the 0° contour is marked dotted. CEOF phase is shown with additional arrows anti-parallel to its gradient to indicate prevailing propagation direction (explanation see text). Ticks mark the beginning of a year

type used to remove the GISST trend but with half-power at 1 year (cf. fig. 8). The domain is restricted to equatorward of 22°, including the Indian ocean. The explained percentage of variance of the complex-valued time-dependent input field in filtered and (parenthesized) in unfiltered form is given; note that by construction the imaginary part of the input has the same variance as the real part. The second and third panels show the amplitude and phase of the complex principal component, below are maps

for amplitude and phase of the leading pattern. An arbitrary constant phase can be added simultaneously to both the component and the spatial phase; for definiteness we imposed orthogonality of the real and the imaginary part of the pattern, with maximum variance in the real part. This constant phase determines the principal component real part shown in the top panel. One should note that no direct constraint for matching the NINO3 SST anomaly timeseries of fig. 6 is imposed, but there is close agreement as expected, because in the reconstruction of the original, real valued process from principal component and pattern the product of their real parts contributes the dominant of two terms.

Zero spatial or component amplitude implies undefined phase and leads to disruptions in component phase, resp. singular points in the spatial phase, as evident for the model. Thus the first point to notice is that locations of small amplitude and close-to-undefined phase agree well in model and observations, or conversely, similar regions contribute dominantly. The patterns in both cases explain about half of the (filtered) variance, and the variance reduction by filtering is similar. The mean amplitude over the central and eastern Pacific in both is also close (note separate but similar scales on the principal components), but the model has 1.2 units near the Peruvian coast where 2.4 are observed; the component and spatial amplitudes combining multiplicatively this implies just less than a factor of 2. The very sharp peak in the simulation on the equator near 120° W corresponds to the surfacing of the isotherms in the equatorial section shown earlier.

A number of higher resolution models miss the true spatial extent of the equatorial zone of maximum SST variance and underestimate it near the coast due mainly to overly strong equatorial upwelling and still insufficient resolution as well as insufficient AGCM simulated windstress near the coast (e.g. Robertson et al. 1995, Latif et al. 1994). In our model, the more important impairment is the standard ocean modelling problem with zonal resolution, which is 2.8 degrees. Further the vertical temperature gradient on the equator is perhaps too strong being represented by not as many layers as would produce a correct vertical distribution of mixing. When gradients relax during a warm heat content anomaly, the SST amplitude is exaggerated. As noted by Roeckner et al. (1996) this has little impact on the atmospheric response due to the spatial confinement.

Included with the spatial phase are arrows parallel to the negative of the phase gradient at arrow base. Since at any point the instantaneous phase is the difference of the component phase and the spatial phase this shows the direction of propagation for lines of constant phase whenever there is a negative rate of change of component phase. Evidently, for both model and observations apparent propagation is confined to regions with insignificant signal strength, maximum variance occurring at virtually constant phase. This reasserts the finding from the Hovmoeller diagrams and confirms for the observations that a standing SST pattern is dominant in ENSO variability. An overall point shared by the two datasets, as already suggested by the explained variance fraction, is that none of the subsequent CEOFs was found to contain ENSO-related variability, the single exception being that the 1982/83 ENSO produces a peak in the second principal component, and correspondingly is slightly weaker in the first.

Regarding the upper ocean heat content (fig. 11), the situation with observed data is considerably more difficult than for SST. The data represents temperature integrated over the upper 400 m as measured by expendable bathythermographs (XBT), gridded to 5° × 2° (lon × lat) after spatial and temporal gaps have been filled (White 1995). We use the full record length but note the increase in samples during the 1970 s and 80 s. Thus when inspecting the component amplitude and phase with some caution, from about 1970 onwards we find quite good accordance with what was seen with the GISST data. The 1972, 1982 and 1986 ENSOs are also clearly present in the real part. Yet the agreement in component time series of SST and heat content is more clearly evident for the simulation results. For both datasets, however, the time series suggest that, apart from data uncertainties we again

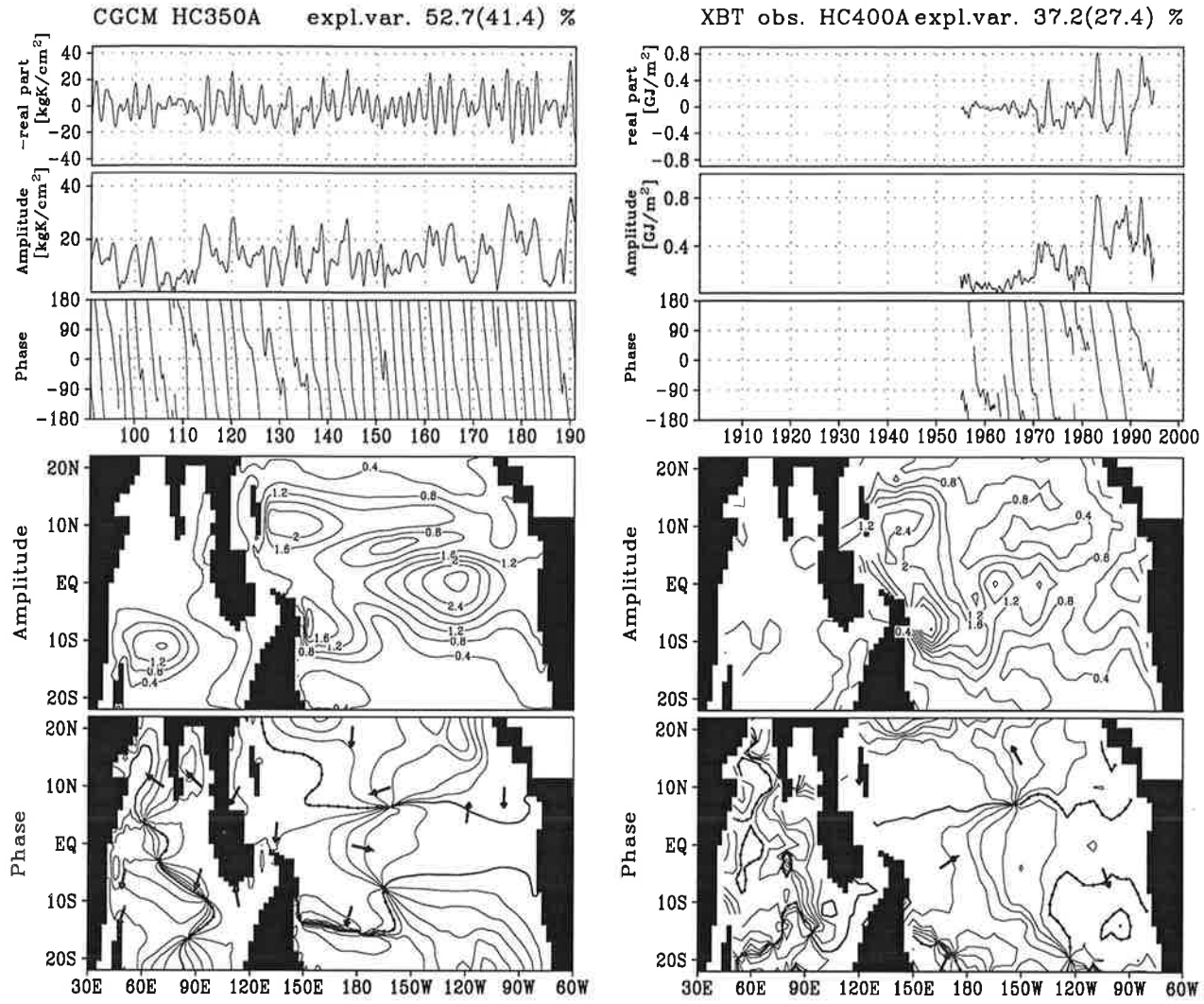

Fig. 11. As fig. 10, but for upper ocean heat content. a) coupled model, upper 350 m (shallower areas omitted), b) XBT data, upper 400 m

capture the ENSO signal remarkably well in the leading CEOF.

Turning to the spatial amplitude and phase, for both model and observations we find a rather similar structure in the western and central Pacific. The zone of maximum amplitude occupies a band of about 10 degrees latitudinal extent centered on the equator, and both datasets show a minimum of similar shape at about 8° N and west of 110° W. North of this minimum, about 10-12° N, we see a prolonged zonal stretch of larger amplitude extending to the western boundary, where peaks of obvious similarity obtain, regarding shape and strength. A western boundary peak is also situated near 5° S. South of this latitude, weak amplitude is associated with phase noise. From this latitude northward, the phase has a pronounced basinscale structure characterized by eastward propagation along the equator separated from a zone of westward propagation north of the aforementioned minimum. The apparently ENSO-related simulated peak in the Indian ocean is not clearly seen in the observations. It corresponds to a structure in zonal windstress and is discussed below.

One could be tempted to combine the rate of change of the temporal phase and the phase gradient to

form estimates of the phase speed e.g. on the equator, which would be larger in the simulation than in the observations, in fact consistent with fig. 9. However, this will be subject to some distortion, since a single temporal phase is responsible for the entire domain, and examination e.g. of the phase lines approaching the western boundary shows that a zone of maximum phase speed would result there. This caveat applies as well to other statistical methods for obtaining time-invariant complex-valued large-scale patterns. Moreover, in such methods a strict decomposition into single baroclinic modes is not achievable, but in the best case, as presented here, one obtains a representation of how on average energy propagates in a set of waves associated with an El Nino. The superposition of more than one wave in an El Nino was indicated earlier by the fine structure in the apparent eastward propagation in fig. 9.

The results of the heat content analysis, on the one hand, confirm the dominance by off-equatorial westward propagation and subsequent western boundary reflection into eastward propagating equatorial signals. The latitude band of westward propagation coincides with the one used in the Hovmoeller diagrams, fig. 9. On the other hand, at any one instant where there is maximum positive or negative eastern equatorial sea level displacement, the off-equatorial displacement in the west is of opposite sign and also close to its extreme. Thus both model and observations apparently agree on the dominant horizontal wave structure and expected equatorial forcing.

The observed windstress from the FSU atlas for the Pacific is used exclusively here since the Indian ocean is only covered from 1970 through 1994. As with the XBT data, in fig.12 the component amplitude and phase, taking into account the weakened phase definition associated with zero or near zero amplitude, show reasonable agreement with those found in the case of the GISST data. It is noteworthy that the pattern contains only a good quarter of the filtered variance. Also, imposing half-power at 1 year already implies eliminating almost three quarters of the unfiltered variance which is not surprising with this atmospheric parameter, though, and feasible in the sense of essentially retaining the ENSO signal. Remarkably, very similar low pass fraction and explained variance percentage result in the simulation. There also, the correspondence between the component phase and amplitude and those of the SST and heat content is again more manifest than in the observations, but the lack of equal length datasets for all our observed quantities in this case implies little more than two decades for comparing GISST and XBT data.

As expected, the pattern of both the observed and the simulated windstress variability is dominated by a maximum on the equator centered virtually on the date line. In the simulation, it appears slightly shifted, between 5 and 10 degrees or two to three gridpoints to the west. The centre regions agree well in strength, while the off-equatorial westward and eastward expanses are simulated stronger than observed. In the eastern Pacific, the maximum evident in the model at 120° W is qualitatively similar to a weak observed structure. Similarly, qualitative agreement is found in the minimum west of this feature, as well as concerning the maximum near 15° S and the minimum near 15° N. The simulated maximum in the Indian ocean is nearly anticorrelated with the maximum at the date line; this phase relationship is consistent with the case of the heat content maximum in that basin whose location is west of the windstress maximum. Since the observed dataset does not cover the Indian ocean, further investigation is in order to ascertain the correspondence with observed variability, as is an analysis of the Indian in isolation, to examine how much distortion possibly results from the inclusion of the strong Pacific ENSO variability.

For the simulation results, the complex cross-correlation functions have maximum modulus at 0 months for SST and heat content, and at 1-2 months lead for windstress relative to heat content (fig.13). The latter is consistent with near zero lag within the limits imposed by the previous low-pass filtering. The component amplitudes shown in fig. 10 through 12 already suggest strong correlations

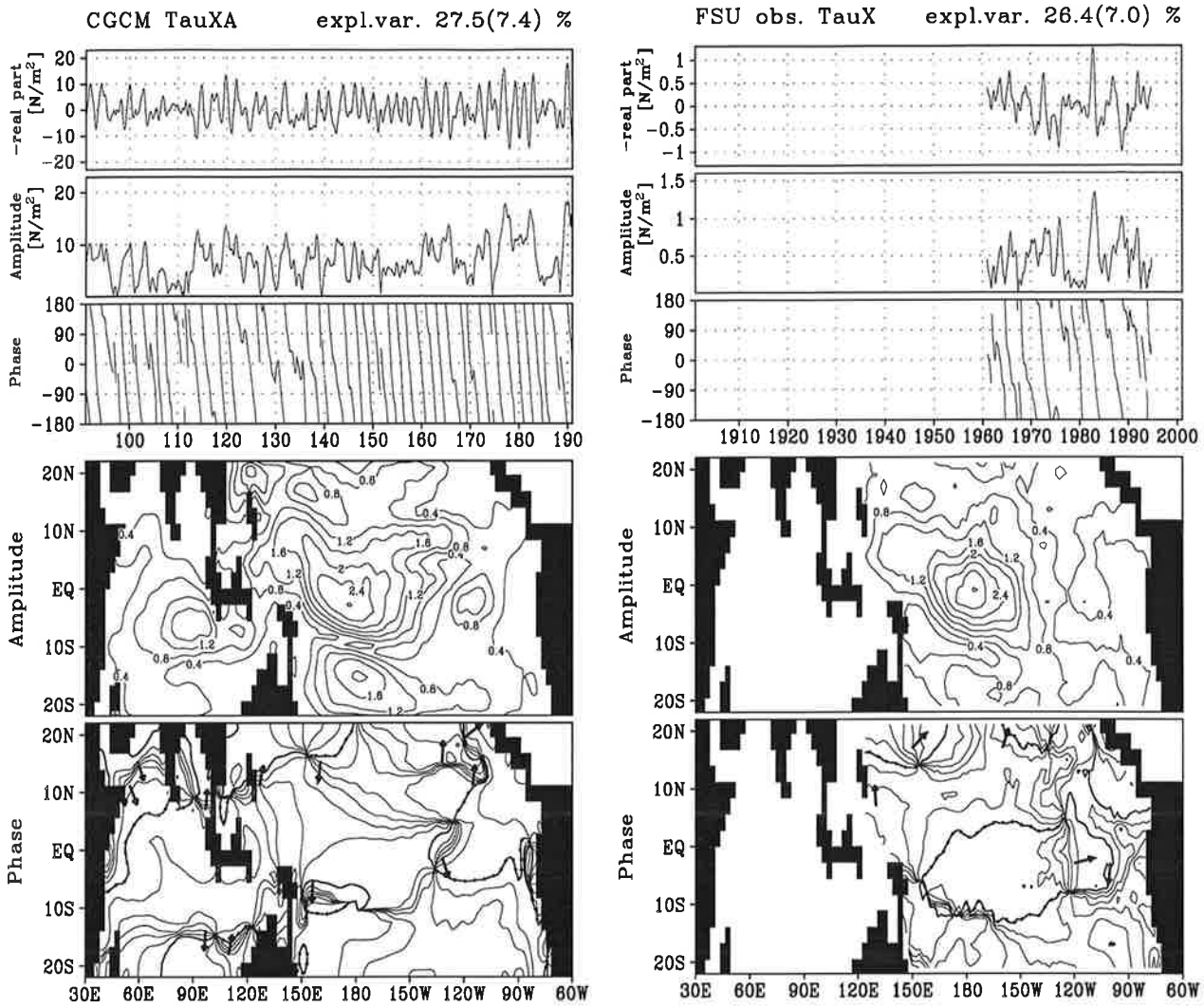

Fig. 12.As fig. 10, but for zonal wind stress. a) coupled model, b) FSU data

(for the phase the arbitrary constants must in principle be considered).

The essentials of the dominant portion of the model ENSO dynamics, as described in the discussion of fig. 9., now re-emerge as follows. Choose locations of peak amplitude in the patterns of SST, windstress, heat content at phase 180°, 150-180°, 0-30°, resp. These phases imply that the time evolution at these locations reconstructed from the leading CEOF resembles the principal component real part, with east Pacific warm SST in phase with westerly windstress anomalies and cold (downwelling) off-equatorial Rossby amplitude (all have the component real part at negative extremes). Corresponding arguments apply to the observed CEOFs for the 1970s and 1980s (with reversed component real part signs and flipped spatial phase).

That the strength and spatial phasing of the ENSO-related variability in the above key parameters emerges so clearly matched between our simulation and observations, suggests that our model captures a major proportion of relevant physics.

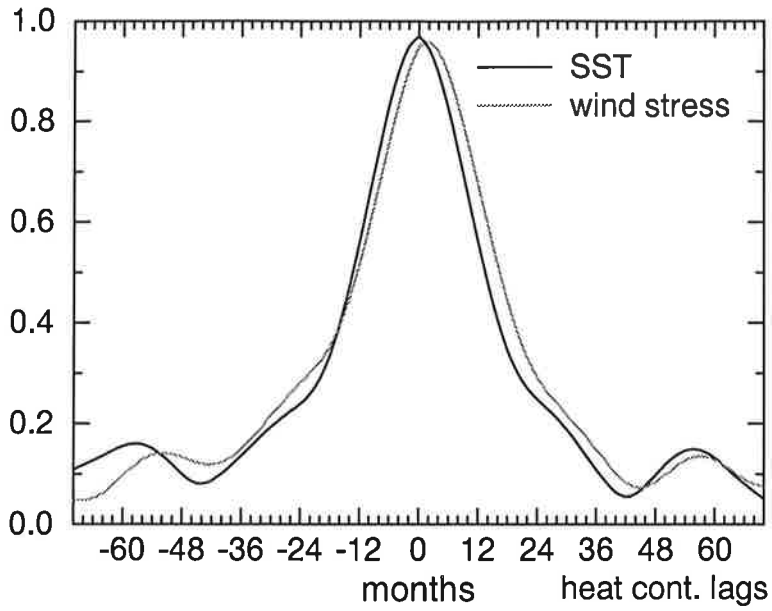

Fig. 13. Modulus of complex correlation of complex principal component time series in the coupled model for heat content - SST (full line), and heat content - zonal wind stress (dotted)

The above-mentioned preference for a timescale of about 28 months, in view of the non-local pattern of atmosphere-ocean interaction, appears unrelated to local biennial mechanisms such as described by Meehl (1992) and others (who emphasize atmospheric convection and concomitant turbulent mixing in the upper ocean). Limited vertical resolution below the thermocline may favour the lowest baroclinic modes. The phasespeeds apparently characteristic in fig. 9 best fit the second mode. However, sub-thermocline resolution comparable to ours is found in the paper by Tett (1995) who describes weak ENSO-like behaviour and a timescale close to three years. There is further complication since coupled ocean-related modes theoretically have structure differing from that of ocean-only modes (cf. the review of theory related to simple and intermediate models in Neelin et al. (1994)).

The timescale preferred by the simulation is also evident from the phase of the principal components of the analyzed variables. A characteristic timescale appears less well-defined in the GISST dataset in which, if anything, from about 1960 to 1990 the phase appears to show a three-year timescale. This leading CEOF is rather stable when we vary the length of the record analyzed. To partially resolve the apparent inconsistency with fig.7, an inspection of the component amplitude suffices, since even weak but nonzero amplitude has an associated phase progression but the spectral peak is largely positioned according to the strongest, somewhat less frequent events. The phase evolution in the observations raises new questions concerning the notion of bimodal spectrum cited at the beginning of the section, since in that case most conceivably the phase would bring out the shortest timescale near 2 years clearly (superposition involving two frequencies could produce alternating sense of phase progression or recurrently more frequent revolutions), or noticeable connections to ENSO should appear in higher patterns. Moreover, the principal component itself shows that even three years, or any sharply defined value, does not appear to be a universally applicable period through this dataset, thus signal identification should also emphasize the spatial aspect as stressed by Barnett et al. (1995) and inherent in our analysis. The CEOF method appears to admit a decription not necessarily preferring discrete damped linear modes under stochastic forcing which are part of the assumptions when applying autoregressive models and the related Principal Oscillation Pattern (POP) analysis (Hasselmann 1988, Latif et al. 1992, Barnett et al. 1995).

5. CONCLUSIONS

We have validated the tropical Pacific seasonal cycle and interannual variability for the first 100 years of a multi-century simulation with a global atmosphere-sea ice-ocean general circulation model which employs non-seasonal heat and freshwater flux adjustment.

The good simulation of the warm pool annual/semiannual cycle is encouraging and is accompanied by a mean state not predominantly forced by the flux adjustment. A major challenge for coupled GCMs, the mean cold tongue extent and the south-eastern extent of the warm pool, is captured. In the east, the lack of realistic spring warming over some two or three grid longitudes is mostly attributable to mixing between surface and cold subsurface layers. Clearly the vertical discretization resulting in typically six layers of space-time dependent depth above 350 m causes some of this difficulty. The chosen number of layers represents a compromise in view of the requirement of an extended ocean spinup integration. On the other hand, we obtain a well-simulated vertical temperature distribution and a rather satisfactory overall current structure, on which to substantially improve would demand significantly higher resolution horizontally as well as vertically.

The AGCM stress is no weaker than observed and has an overall realistic pattern, and this is what makes it feasible to abandon flux adjustment for windstress altogether. This is important for the links between simulated seasonal cycle and ENSO variability, since especially seasonal windstress adjustments can distort the phasing of equatorial windstress anomalies, as discussed in Neelin et al. (1992). Also, Neelin and Dijkstra (1995) in an intermediate model obtain a bifurcation of a single stable state of tropical SST climatology into a bistable system with one rather realistic state and one with unrealistically high eastern Pacific SST when flux adjustment of the windstress is introduced with varying strength. Simulation of ENSO dynamics could thus become strongly distorted.

For sea surface temperature, zonal windstress and upper ocean heat content, the model captures the dominant amplitude and phase patterns of the observed tropical Pacific ENSO signal as well as its strength. The dominant mechanism in the model is the non-local feedback by windstress responding to anomalous zonal SST gradient and forcing off-equatorial waves that reflect into eastward traveling equatorial Kelvin waves which ultimately reverse the SST anomaly. The obvious match of simulated and observed most prominent patterns of interannual variability is the main reason presented here for identifying the signal in the simulation as ENSO. A validation of the global atmospheric response against the response of the AGCM to interannually varying observed SST was performed by Roeckner et al. (1996). Not unlikely connected to a truncation of the baroclinic mode spectrum, more frequent and not quite as irregular ENSO oscillations are simulated than observed. As to ENSO timescales, our analysis of anomalies in model and observations finds essentially a single amplitude/phase pattern and associated amplitude/phase timeseries, with time evolution most naturally described by a single maximum over a relatively broad frequency range rather than two or more narrowly defined frequencies, though the latter alternative cannot statistically be ruled out.

ACKNOWLEDGEMENTS

This work has benefited a great deal from Prof. Lennart Bengtsson's continued interest and support, as well as his suggestions which led to various improvements in the manuscript. Part of this study was completed during a visit to the Scripps Institution of Oceanography, La Jolla, California, where support in both technical and scientific sense is gratefully acknowledged by A.B., as are the enjoyable and stimulating discussions with Timothy P. Barnett, Niklas Schneider and Arthur J. Miller. The XBT da-

ta were made available by W. B. White, Scripps Institution of Oceanography. The GISST dataset was provided by the British Meteorological Office. The initial coupled segment preceding the main model integration was tended by Ingo Kirchner of the Max-Planck-Institut für Meteorologie (MPI), Hamburg. Stimulation further came from discussion with Hans Graf and Mojib Latif, both MPI. The model integration and much of the analysis were carried out on the Cray-C90 of the Deutsches Klimarechenzentrum (DKRZ), Hamburg. Financial support was given by the Bundesminister für Bildung und Forschung (BMBF) through the project 'Klimavariabilität und Signalanalyse', grant No. 07VKV01/1.

REFERENCES

Bacher A, Oberhuber JM (1996) Global coupling in the ECHAM4/OPYC3 atmosphere-sea ice-ocean GCM with annual mean flux adjustment restricted to heat and freshwater. MPI report, Max-Planck-Institut für Meteorologie, Hamburg, Germany, in preparation

Barnett TP (1983) Interaction of the monsoon and Pacific trade wind systems at interannual time scales. Part I: the equatorial zone. Mon Wea Rev 111: 756-773

Barnett TP, Latif M, Graham NE, Flügel M (1992) Modal structure of variations in the tropical climate system. Part II: Origins of the low-frequency mode. MPI report 96, Max-Planck-Institut für Meteorologie, Hamburg, Germany

Barnett TP, Latif M, Kirk E, Roeckner E (1991) On ENSO physics. J Climate 4: 487-515

Barnett TP, Latif M, Graham N, Flügel M, Pazan S, White W (1993) ENSO and ENSO-related predictability. Part I: Prediction of equatorial Pacific sea surface temperature with a hybrid coupled ocean-atmosphere model. J Climate 6: 1545-1566

Barnett TP, Latif M, Graham N, Flügel M (1995) On the frequency-wavenumber structure of the tropical ocean/atmosphere system. Tellus 47A: 998-1012

Battisti DS, Hirst AC (1989) Interannual Variability in a Tropical Atmosphere-Ocean Model: Influence of the Basic State, Ocean Geometry and Nonlinearity. J Atm Sci 46(12): 1687-1712

Brillinger DR (1981) Time series-data analysis and theory. Holden-Day, 540 pp

Brinkop S, Roeckner E (1995) Sensitivity of a general circulation model to parameterizations of cloud turbulence in the atmospheric boundary layer. Tellus 47A: 197-220

Chen C-T, Roeckner E (1996a) Validation of the Earth radiation budget as simulated by the Max Planck Institute for Meteorology general circulation model ECHAM4 using satellite observations of the Earth Radiation Budget Experiment. J Geophys Res 101, 4269-4287

Chen C-T, Roeckner E (1996b) Warm pool heat budget as simulated by different versions of the ECHAM model. NATO ASI series, Vol. I 34: 95-105

Cubasch U, Hasselmann K, Höck H, Maier-Reimer E, Mikolajewicz U, Santer BD, Sausen R (1992) Time-dependent greenhouse warming computations with a coupled ocean-atmosphere model.

Clim Dyn 8: 55-69

Giorgetta M, Wild M (1995) The water vapour continuum and its representation in ECHAM-4. MPI report 162, Max-Planck-Institut für Meteorologie, Hamburg, Germany

Haney RL (1971) Surface thermal boundary condition for ocean circulation models. J Phys Oceanogr 1: 241-248

Hasselmann K (1988) PIPs and POPs: the reduction of complex dynamical systems using principal interaction and oscillation patterns. J Geophys Res 93: 11015-11021

Hibler WD III (1979) A dynamic thermodynamic sea ice model. J Phys Oceanogr 9: 815-846

Horel JD (1982) On the annual cycle of the tropical Pacific atmosphere and ocean. Mon Wea Rev 110: 1863-1878

Horel JD (1984) Complex principal component analysis: theory and examples. J Climate Appl Met 23: 1660-1673

Jin FF, Neelin JD, Ghil M (1994) El Nino on the devil's staircase: Annual subharmonic steps to chaos. Science 264: 70-72

Kay SM, Marple SL (1991) Spectrum analysis - a modern perspective. Proc IEEE 69(11): 1380-1419

Knutson TR, Manabe S (1994) Impact of increased CO2 on simulated ENSO-like phenomena. Geophys Res Lett 21: 2295-2298

Latif M, Barnett TP, Mizuno K (1992) Modal structure of variations in the tropical climate system. Part I: Observations. MPI report 91, Max-Planck-Institut für Meteorologie, Hamburg, Germany

Latif M, Stockdale T, Wolff J., Burgers G., Maier-Reimer E., Junge M., Arpe K., Bengtsson L. (1994a): Climatology and variability in the ECHO coupled GCM. Tellus 46A: 351-366

Latif M, Barnett TP (1994) Causes of decadal climate variability over the North Pacific and North America. Science 266: 634-637

Lau NC, Philander SGH, Nath MJ (1992) Simulation of El Nino/Southern Oscillation phenomena with a low-resolution coupled general circulation model of the global ocean and atmosphere. J Climate 5: 284-307

Levitus S (1982) Climatological atlas of the World Ocean. NOAA Prof. Paper No. 13, U.S. Government Printing Office, Washington, D.C., 173 pp

Lunkeit F, Sausen R, Oberhuber JM (1996) Climate simulations with the global coupled atmosphere-ocean Model ECHAM2/OPYC. Part I: Present-day climate and ENSO events. Clim Dyn 12: 195-212

Manabe S, Stouffer RJ, Spelman MJ, Bryan K (1991) Transient responses of a coupled ocean-atmosphere model to gradual changes of CO2. Part I: annual mean response. J Climate 4: 785-818

Mechoso CR, Robertson AW, Barth N, Davey MK, Delecluse P, Gent PR, Ineson S, Kirtman B, Latif M, le Treut H, Nagai T, Neelin JD, Philander SGH, Polcher J, Schopf PS, Stockdale T, Suarez MJ, Terray L, Thual O., Tribbia JJ (1995) The seasonal Cycle over the Tropical Pacific in Coupled Ocean-Atmosphere General Circulation Models. Mon Wea Rev 123: 2825-2838.

Meehl GA (1992) A coupled air-sea biennial mechanism in the tropical Indian and Pacific regions: role of the ocean. J Clim 6: 31-41

Morcrette JJ (1991) Radiation and cloud radiative properties in the European Centre for Medium Range Weather Forecasts forecasting system. J Geophys Res 96: 9121-9132

Murphy JM (1995) Transient response of the Hadley Centre coupled ocean-atmosphere model to increasing carbon dioxide. Part I: control climate and flux adjustment. J Climate 8: 36-80

Nagai T, Tokioka T, Endoh M, Kitamura Y (1992) El Nino-Southern Oscillation simulated in an MRI atmosphere-ocean coupled general circulation model. J Climate 5: 1202-1233

Neelin JD (1991): The slow sea surface temperature mode and the fast wave limit: analytic theory for tropical interannual oscillations and experiments in a hybrid coupled model. J Atmos Sci 48: 584-606

Neelin JD, Dijkstra HA (1995) Ocean-Atmosphere Interaction and the Tropical Climatology. Part I: The Dangers of Flux Correction. J Climate 8: 1325-1342

Neelin JD, Latif M, Alaart MAF, Cane MA, Cubasch U, Gates WL, Gent PR, Ghil M, Gordon C, Lau NC, Mechoso CR, Meehl GA, Oberhuber JM, Philander SGH, Schopf PS, Sperber KR, Sterl A, Tokioka T, Tribbia J, Zebiak SE (1992) Tropical air-sea interaction in general circulation models. Clim. Dynamics 7: 73-104

Neelin JD, Latif M, Jin FF (1994) Dynamics of coupled ocean atmosphere models: The Tropical Problem. Ann Rev Fluid Mech 26: 617-659

Nordeng TE (1996) Extended versions of the convective parameterization scheme at ECMWF and their impact on the mean and transient activity of the model in the tropics. Quart J Roy Met Soc (subm.)

Oberhuber (1988) An atlas based on the 'COADS' dataset: The budgets of heat, buoyancy and turbulent kinetic energy at the surface of the global ocean. MPI report 15, Max-Planck-Institut für Meteorologie, Hamburg, Germany

Oberhuber JM (1993) Simulation of the Atlantic circulation with a coupled sea-ice mixed layer-isopycnal general circulation model. Part I: Model description. J Phys Oceanogr 13: 808-829

Parzen E (1961) Mathematical considerations in the estimation of spectra. Technometrics 3, 167-190

Philander SGH, Pacanowski RC, Lau NC, Nath MJ (1992) Simulation of ENSO with a Global Atmospheric GCM Coupled to a High-Resolution, Tropical Pacific Ocean GCM. J Climate 5: 308-329

Picaut J, Tournier R (1991) Monitoring the 1979-1985 equatorial Pacific current transports with expendable bathythermograph data. J Geophys Res 96, suppl: 3263-3277

Rasmusson EM, Wang X, Ropelewski CF (1990) The biennial component of ENSO variability. J Mar Sys 1: 71-90

Rayner NA, Folland CK, Parker DE, Horton EB (1995) pers. comm. (A new global sea-ice and sea surface temperature (GISST) data set for 1903-1994 for forcing climate models, Hadley Centre internal note No. 69)

Reverdin G, Frankignoul C, Kestenare E, McPhaden MJ (1994) Seasonal variability in the surface currents of the equatorial Pacific. J Geophys Res 99, C10: 20323-20344

Reinsch CH (1967) Smoothing by spline functions. Numerische Mathematik 10: 177-183

Robertson AW, Ma CC, Mechoso CR, Ghil M (1995a) Simulation of the tropical Pacific Climate with a coupled ocean-atmosphere general circulation model. Part I: The seasonal cycle. J Climate 8: 1178-1198

Robertson AW, Ghil M, Mechoso CR (1995b) Simulation of the tropical Pacific Climate with a coupled ocean-atmosphere general circulation model. Part II: Interannual variability. J Climate 8: 1199-1216

Roeckner E, Oberhuber JM, Bacher A, Christoph M, Kirchner I (1996) ENSO variability and atmospheric response in a global coupled atmosphere-ocean GCM. Clim Dyn (accepted)

Roeckner E, Arpe K, Bengtsson L, Brinkop S, Dümenil L, Esch M., Kirk E., Lunkeit F, Ponater M, Rockel B, Sausen R, Schlese U, Schubert S, Windelband M (1992): Simulation of the Present-day climate with the ECHAM model: Impact of model physics and resolution. MPI report 93, Max-Planck-Institut für Meteorologie, Hamburg, Germany

Sausen R, Bartel K, Hasselmann K (1988) Coupled ocean-atmosphere models with flux correction. Clim. Dyn. 2: 145-163

Sausen R, Schubert S, Dümenil L (1994) A model of river run-off for use in coupled atmosphere-ocean models. J Hydrology 155: 337-352

Schneider N, Barnett TP (1995) The Competition of Freshwater and Radiation in Forcing the Ocean during El Nino. J Climate 8: 980-992

Schopf PS, Suarez MJ (1988): Vacillations in a coupled ocean-atmosphere model. J Atmos. Sci. 45: 549-566

Suarez MJ, Schopf PS (1988): A delayed action oscillator for ENSO. J Atmos Sci 45: 3283-3287

Stricherz JN, O'Brien JJ, Legler DM (1992) Atlas of Florida State University tropical Pacific winds for TOGA 1966-1985. The Florida State University, Mesoscale Air-Sea Interaction Group, Tallahassee, Florida

Stricherz JN, O'Brien JJ, Legler DM (1993) Atlas of Florida State University Indian Ocean winds for TOGA 1970-1985. The Florida State University, Mesoscale Air-Sea Interaction Group, Tallahassee, Florida

Tett S (1995) Simulation of El Nino-Southern Oscillation-like Variability in a Global AOGCM and its response to CO2 Increase. J Climate 8: 1473-1502

White WB (1995) Design of a global observing system for gyre-scale upper ocean temperature variability. Progress in Oceanography 36(3): 169-217

Wyrtki K, Kilonsky B (1984) Mean water and current structure during the Hawai-to-Tahiti Shuttle Experiment, J Phys Oceanogr 14: 242-254